Boundary-Layer Meteorology (2024) 190:15
https://doi.org/10.1007/s10546-024-00858-w

RESEARCH ARTICLE

A Reinterpretation of Phenomenological Modeling Approaches for Lagrangian Particles Settling in a Turbulent Boundary Layer

Andrew P. Grace[1] · David H. Richter[1] · Andrew D. Bragg[2]

Received: 25 July 2023 / Accepted: 13 February 2024

Abstract
It has long been known that under the right circumstances, inertial particles (such as sand, dust, pollen, or water droplets) settling through the atmospheric boundary layer can experience a net enhancement in their average settling velocity due to their inertia. Since this enhancement arises due to their interactions with the surrounding turbulence it must be modelled at coarse scales. Models for the enhanced settling velocity (or deposition) of the dispersed phase that find practical use in mesoscale weather models are often ad hoc or are built on phenomenological closure assumptions, meaning that the general deposition rate of particles is a key uncertainty in these models. Instead of taking a phenomenological approach, exact phase-space methods can be used to model the physical mechanisms responsible for the enhanced settling, and these individual mechanisms can be estimated or modelled to build a more general parameterization of the enhanced settling of inertial particles. In this work, we use direct numerical simulations (DNS) and phase-space methods as tools to evaluate the efficacy of phenomenological modeling approaches for the enhanced settling velocity of inertial particles for particles with varying friction Stokes numbers and settling velocity parameters. We use the DNS data to estimate profiles of a drift–diffusion based parameterization of the fluid velocity sampled by the particles, which is key for determining the settling velocity behaviour of particles with low to moderate Stokes number. We find that by increasing the settling velocity parameter at moderate friction Stokes number, the magnitude of preferential sweeping is modified, and this behaviour is explained by the drift component of the aforementioned parameterization. These profiles indicate that that when eddy-diffusivity-like closures are used to represent turbulent transport, empirical corrections used in phenomenological models may be potentially compensating for their incompleteness. Finally, we discuss opportunities for reinterpreting phenomenological approaches for use in coarse-scale weather models in terms of the exact phase-space approach.

✉ Andrew P. Grace
agrace4@nd.edu

[1] Civil and Environmental Engineering and Earth Sciences, University of Notre Dame, Notre Dame, IN 46556, USA

[2] Department of Civil and Environmental Engineering, Duke University, Durham, NC 27708, USA

Published online: 22 March 2024

Keywords Multiphase flows · Turbulent boundary layer · Inertial particles · Mathematical modeling · Direct numerical simulations · Atmospheric surface layer

1 Introduction

A detailed and fundamental understanding of the processes responsible for the dispersion of dust and sand particles (about 0.5–100 μm in size (Kok et al. 2012; Shao 2008)) in the atmospheric boundary layer is of utmost importance for accurate modeling of their impact on biogeochemical cycles (Ryder et al. 2018), global radiation balance (Miller et al. 2006), air quality (Querol et al. 2019), and a host of other processes. More fundamentally, the interactions between dust particles and turbulent air present an interesting and important multi-scale physics and engineering problem. Dust and sand particles are emitted from the ground through a series of complex interactions between gravity, wind stresses from synoptic-scale events, electrostatic forces, and other dynamic forces (Kok et al. 2012). Under certain circumstances, these particles may rise high into the atmosphere (Kok et al. 2017) and be transported thousands of kilometers away (Shao 2008) (depending on their size). Part of the challenge of predicting the global transport in the atmosphere is accurate prediction of the rate at which particles of different sizes settle out of the atmosphere under the action of gravity (through their Stokes settling velocity), and how different scales of turbulent motion in the planetary boundary layer (PBL) either enhance or suppress this process.

It has long been known that under net settling conditions, heavy particles settling through turbulence can experience a net enhancement in their average settling velocity, and many studies have linked this to their inertia (Wang and Maxey 1993; Aliseda et al. 2002; Good et al. 2014; Brandt and Coletti 2022). A particle's inertia is quantified by its Stokes number, which is the ratio between the particle's relaxation timescale, and a fluid timescale. A related parameter is the settling velocity parameter, which is the ratio of the Stokes settling velocity to a characteristic fluid velocity. Settling velocity enhancement comes from a variety of sources, but pertinent to the work presented here is the preferential sweeping mechanism (Wang and Maxey 1993; Tom and Bragg 2019), which says that when the turbulence is locally homogeneous and there are no mean gradients in the turbulence properties, inertial particles settling under the force of gravity preferentially sample the downward side of turbulent eddies. This means that on average, the fluid velocities they sample are negative, which leads to an enhancement of the average settling velocity above what would be predicted by the Stokes settling velocity. It can be difficult to observe the enhanced settling velocity due to preferential sweeping in the natural environment, but nevertheless, Nemes et al. (2017) and Li et al. (2021) presented field observations of snowflakes falling through a neutral boundary layer that had fall speeds much higher than their estimated Stokes settling velocity, and they argued that the enhancement was due to preferential sweeping.

Understanding and being able to predict the magnitude of this effect as a function of Stokes number and settling velocity parameter is of utmost importance for accurate modeling of both the horizontal and vertical dispersion of particles and aerosols. Since the magnitude of the interactions between the particles and turbulent eddies are not known a priori, they must be modelled. On the one hand, in controlled numerical and laboratory experiments, empirical expressions for the enhanced settling velocity in terms of the Stokes number, settling parameter and Reynolds number have been proposed for homogeneous isotropic turbulence (Rosa et al. 2016). Meanwhile, models for the enhanced settling velocity (or deposition) of the dispersed phase that find practical use in mesoscale weather models (a list

of which can be found in Kukkonen et al. (2012)) are often quite simple and ad hoc or are built on phenomenological closure assumptions, such as representing the enhancing effects on particle transport by turbulence through an eddy diffusivity approximation, discussed more below. This means that the average settling rate of particles is a key uncertainty in these models in general. Even simpler models in use may take a crude approach, which, roughly speaking, represents the enhanced settling velocity as a sum of the Stokes settling velocity and an additive correction based on the collection efficiencies of various land use categories (Slinn and Slinn 1980; Slinn 1982; Zhang 2001; Emerson et al. 2020; Farmer et al. 2021). These approaches are known as resistance-based approaches, and are discussed at length in Seinfeld and Pandis (1998).

Instead of these ad hoc resistance approaches, others have developed relationships between the surface flux and mean concentration profile which are based on the conservation equations for particle concentration. In the limit of assuming that the diffusive effects of turbulence on the particles are in exact balance with gravitational settling, one arrives at the so-called "Rouse profile" (Rouse 1937; Prandtl 1952; Boudreau and Hill 2020). This simple power-law profile has been extended for non-equilibrium conditions (meaning a net constant downward or upward flux) (Hoppel 2005; Kind 1992) and non-neutral atmospheric stability (Freire et al. 2016). The Rouse profile serves as a yardstick by which to compare high Reynolds number laboratory experiments (Berk and Coletti 2020) and direct numerical simulations (Richter and Chamecki 2018), but is only accurate in the limit of vanishing inertia. Corrections to account for the effect of particle inertia in the near-wall region (the viscous sub-layer) have been applied to the mass conserving approach. The common application is to practically model a process known as impaction, which is the term used to refer to the rate at which settling particles impact a canopy element based on their ability to adjust to changes in fluid streamlines, which is a function of the particle inertia (Emerson et al. 2020). Thus the degree to which inertia is relevant to a particle's settling behaviour in phenomenological models is often contained within the impaction component of the model. In order to parameterize the effect of different land use categories on the settling behaviour (such as grasslands, forests, and water surfaces, for example) empirical corrections and significant model calibration are required, as the details can vary significantly depending on the land use category (Zhang 2001; Farmer et al. 2021).

As an alternative to the phenomenological approaches discussed above, exact phase-space methods which quantify the evolution of the probability density function of an ensemble of particles, such as that outlined in Pope (2000), can be used to explicitly represent the settling velocity as the sum of distinct mechanisms which can be estimated or modelled to build a more general parameterization of the enhanced settling of inertial particles. In a recent paper, Bragg et al. (2021a) used this approach to identify the important mechanisms governing particle settling in coupled direct numerical simulations of a turbulent boundary layer and Lagrangian point particles for negative net flux (settling) conditions. They computed averaged profiles of each of the terms, confirming that for settling conditions within the interior of the turbulent boundary layer (what they refer to as the quasi-homogeneous region), the dominant settling mechanisms for low and moderate Stokes number were the Stokes settling velocity and preferential sweeping. At higher Stokes number, they additionally identified turbophoresis as an important mechanism. Finally, they discussed the necessity of a drift–diffusion type closure (Reeks 1992; Skartlien 2007; Bragg et al. 2012b) for modeling the fluid velocities sampled by the settling particles, though they do not quote an exact form.

In this paper, we take inspiration from Bragg et al. (2021a) and discuss two different approaches for modeling the settling of inertial particles through turbulent boundary layers at different friction Stokes numbers (St^+) and settling velocity parameters (Sv^+). The first

approach is based on the phase-space probability of the ensemble of particles discussed in both Bragg et al. (2021a) and Skartlien (2007). This method is exact but unclosed; we adopt the drift–diffusion closure discussed in Reeks (1992) to model the fluid velocities sampled by the particle. We then use the DNS data to assist in estimating the magnitude and the overall behaviour of the components of this closure across the quasi-homogeneous region of the turbulent boundary layer for varying St^+ and Sv^+. We then consider a phenomenological but mass-conserving approach discussed in Hoppel (2005) and Giardina and Buffa (2018). This approach is similar to the ad hoc resistance based approaches discussed earlier. The phenomenological approach is based on an eddy-diffusivity closure for the turbulent flux of particles, which allows us to solve the governing differential equation for an equation for average vertical particle velocity at a reference height. We show that while these ad hoc approaches might provide reasonable deposition estimates, the approach they take is fundamentally inappropriate as they are assuming a priori that the turbulent fluxes can be modelled specifically as a diffusive process, and not one that includes a drift component. We then discuss the implications of the different approaches for modeling the settling of inertial particles and recommend improvements that have potential to be implemented in operational models.

In Sect. 2 we introduce the numerical model, and the equations of motion for both the carrier phase and the dispersed phase, and finally outline the series of Numerical Experiments for the rest of the work. Section 3 outlines the phase-space and closure assumption that will be employed in the paper, as well as details regarding the phenomenological modeling approach that will serve as a comparative lens by which to view the results. Section 4 highlights the results for the two Numerical Experiments described in Sect. 2, and finally Sect. 5 provides a brief summary of the results and a discussion of the comparison between the two modeling approaches.

2 Model Setup

2.1 Carrier Phase

In this work, we use the NCAR Turbulence with Lagrangian Particles Model (NTLP) to model one-way coupled inertial particles settling through a turbulent boundary layer, which has been used for numerous particle-laden turbulence studies (Richter and Chamecki 2018; Wang et al. 2019; Gao et al. 2023). For the carrier phase, we use direct numerical simulations (DNS) to solve the three dimensional incompressible constant density Navier-Stokes equations in a turbulent open channel flow setup:

$$\frac{D\boldsymbol{u}}{Dt} = -\frac{1}{\rho_a}\nabla p + \nu\nabla^2\boldsymbol{u} - \frac{1}{\rho_a}\frac{dP}{dx}\hat{\boldsymbol{x}}, \tag{1}$$

$$\nabla \cdot \boldsymbol{u} = 0. \tag{2}$$

A schematic of the setup is presented in Fig. 1. In the above equations, $\frac{D}{Dt}$ represents the material derivative, $\boldsymbol{u}$ represents the three dimensional flow velocity, p represents the turbulent pressure field, ρ_a is the air density, and ν is the kinematic viscosity. The flow is one-way coupled, meaning that the flow does not feel the effects of the dispersed phase.

At the lower boundary, a no-slip boundary condition is enforced, while at the upper boundary, a no-stress boundary condition is enforced. The domain is periodic in the x and y directions. The background state of the carrier phase is established by accelerating the

flow with an imposed pressure gradient, $-dP/dx > 0$ (note that $\hat{\boldsymbol{x}}$ is the unit vector in the streamwise direction) and allowing the flow to become turbulent. The magnitude of the pressure gradient allows us to define a friction velocity $u_\tau = \sqrt{\tau_w/\rho_a}$, where τ_w is the stress at the lower boundary. Using the friction velocity, the height of the domain, H, and viscosity of the carrier phase, we can define a friction Reynolds number of $\mathrm{Re}_\tau = \frac{u_\tau H}{\nu}$. Friction Reynolds numbers for each simulation presented in this work can be found in Tables 1 and 2.

2.2 Dispersed Phase

For each particle (the dispersed phase), we apply the point-particle approximation and solve the conservation of momentum for a rigid spherical particle subjected to linear hydrodynamic drag and the gravitational force:

$$\frac{d\boldsymbol{v}_p}{dt} = \frac{1}{\tau_p}\left(\boldsymbol{u}_p - \boldsymbol{v}_p\right) - \boldsymbol{g}, \tag{3}$$

$$\frac{d\boldsymbol{x}_p}{dt} = \boldsymbol{v}_p. \tag{4}$$

Here, $\boldsymbol{v}_p$ represents the three dimensional velocity vector of each particle, $\boldsymbol{x}_p$ is the location of each particle, $\boldsymbol{g}$ is the gravitational acceleration (which only affects accelerations in the z direction), $\boldsymbol{u}_p$ is the flow velocity evaluated at the location of the particle, and τ_p is the relaxation timescale of the particle, defined as:

$$\tau_p = \frac{\rho_p d_p^2}{18\rho_a \nu}, \tag{5}$$

where ρ_p is the particle density and d_p is the particle diameter.

Once the system is at equilibrium, a vertically constant mass flux is maintained by injecting Lagrangian particles at the upper boundary of the domain with a downward vertical velocity equal to their Stokes settling velocity ($\tau_p g$) at a random horizontal location. Particles are removed from the domain once they contact the bottom boundary, ensuring that a new particle is re-injected after one is removed thereby maintaining a constant particle number. Particles are also allowed to rebound elastically from the upper boundary, though this happens rarely.

Using the friction velocity and the kinematic viscosity of the carrier phase, we can non-dimensionalize the particle diameter, particle relaxation timescale, and the Stokes settling velocity;

$$d^+ = \frac{d_p u_\tau}{\nu}, \quad \mathrm{St}^+ = \frac{\tau_p u_\tau^2}{\nu}, \quad \mathrm{Sv}^+ = \frac{\tau_p g}{u_\tau}. \tag{6}$$

For the rest of this study, the normalized particle diameter (which can also be interpreted as a particle Reynolds number) is held fixed at $d^+ = 0.236$. St^+ is a viscous Stokes number and quantifies the inertia of the particle. Sv^+ is the settling velocity parameter, which with this definition is directly related to the Rouse number from Rouse-Prandtl theory (Rouse 1937; Prandtl 1952). Finally, we will also refer to the integral Stokes number $\mathrm{St} = \tau_p/\tau_L$, where τ_L is the Lagrangian integral timescale (also known as the Lagrangian timescale of turbulence). For a turbulent boundary layer, the Lagrangian integral timescale increases with height as turbulent motions higher in the boundary layer are highly correlated with themselves for longer. More information on the computation of this parameter can be found in Sect. 3.1.

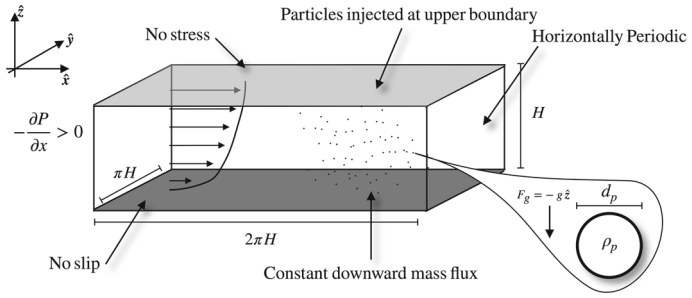

Fig. 1 The domain is a rectangular channel of height H, streamwise length $2\pi H$ and spanwise width πH. The carrier phase is subjected to a constant pressure gradient in the streamwise direction, and the boundary conditions enforced at the top and bottom boundaries are no-stress and no-slip respectively, while the horizontal boundary conditions are periodic. Particles are injected at the upper boundary at a random horizontal location with an initial velocity equal to $\tau_p g$ and removed when they contact the bottom boundary. They are allowed to rebound elastically off the upper boundary

2.3 Numerical Experimental Setup

In this manuscript, we take two Numerical Experimental approaches. The first is to vary St^+ and Sv^+ independently, and parameter values for these cases can be found in Table 1. This has been done in several studies focusing on the dominant mechanisms responsible for inertial particle settling in turbulent boundary layers (Bragg et al. 2021a, b) and homogeneous isotropic turbulence (Wang and Maxey 1993; Rosa et al. 2016). Practically speaking, to choose St^+, we vary the particle density, ρ_p, whereas to choose Sv^+, we vary the magnitude of the gravitational acceleration, g. Thus, in addition to the relaxation timescale τ_p, there is a second timescale associated with Sv^+ that is proportional to $\tau_s = \sqrt{\ell g^{-1}}$, where ℓ is some length scale.

The second experimental approach we take is to couple St^+ and Sv^+ though a parameter we denote as Γ. When studying particle deposition processes in geophysical contexts (i.e. deposition over the ocean, glaciers, tundras, forest canopies, etc.), g is not a free parameter, and Sv^+ and St^+ are not independent but are instead linked through characteristics of the turbulent flow (i.e. a known ν, u_τ, and g). Thus a particle's inertia and its settling velocity are physically coupled, and can be written: $\mathrm{Sv}^+ = \Gamma \mathrm{St}^+$, where $\Gamma = \nu g / u_\tau^3$. In order to make a comparison between our work and pre-existing work on the deposition of inertial particles, we include several cases where St^+ and Sv^+ are not varied independently. Parameter values for these cases are shown in Table 2.

The cases in Table 1 were chosen to have $\mathrm{Re}_\tau = 630$, while the cases in Table 2 have $\mathrm{Re}_\tau = 315$, which is the same Re_τ as the simulations presented in Bragg et al. (2021a). It is well known that a there is a significant portion of the flow at both these Reynolds numbers that exhibit the traditional logarithmic behaviour in the quasi-homogeneous layer (Kantha and Clayson 2000; Bragg et al. 2021a), so we do not expect any significant Reynolds number dependence between the two sets of cases.

3 Models of Particle Deposition

In this section, we will highlight some of the main details of the two modeling approaches for the deposition of inertial particles in a turbulent boundary layer, with specific interest in

Table 1 The above table highlights the experiments discussed in Sect. 3.1

Re_τ	Sv^+	St^+	Γ	$N_x \times N_y \times N_z$
630	0.025	0.1	0.25	$256 \times 256 \times 256$
630	0.025	10	0.0025	$256 \times 256 \times 256$
630	0.025	100	0.00025	$256 \times 256 \times 256$
630	0.1	0.1	1	$256 \times 256 \times 256$
630	0.1	10	0.01	$256 \times 256 \times 256$
630	0.1	100	0.001	$256 \times 256 \times 256$
630	0.25	0.1	2.5	$256 \times 256 \times 256$
630	0.25	10	0.025	$256 \times 256 \times 256$
630	0.25	100	0.0025	$256 \times 256 \times 256$

We will refer to this set of simulations as "Numerical Experiment 1". Re_τ is the friction Reynolds number, Sv^+ is the settling velocity parameter in terms of viscous units, St^+ is the Stokes number in terms of viscous units, Γ is the ratio of Sv^+ and St^+, and $N_x \times N_y \times N_z$ are the number of grid points in the streamwise, spanwise, and vertical directions respectively. For this experiment, St^+ and Sv^+ are independently varied

Table 2 The above table highlights the experiments discussed 3.3

Re_τ	Sv^+	St^+	Γ	$N_x \times N_y \times N_z$
315	0.00025	0.1	0.0025	$128 \times 128 \times 128$
315	0.0025	1	0.0025	$128 \times 128 \times 128$
315	0.025	10	0.0025	$128 \times 128 \times 128$
315	0.25	100	0.0025	$128 \times 128 \times 128$
315	0.0001	0.1	0.001	$128 \times 128 \times 128$
315	0.001	1	0.001	$128 \times 128 \times 128$
315	0.01	10	0.001	$128 \times 128 \times 128$
315	0.1	100	0.001	$128 \times 128 \times 128$

We will refer to this set of simulations as "Numerical Experiment 2". The Parameters take the same definitions as those discussed in Table 1. Note that in these cases St^+ and Sv^+ are coupled, meaning that Γ is held constant for each subset of cases

the dominant behaviour in the log layer. This layer is often taken to represent to lowest 100 m of the atmospheric boundary layer, and its characteristics are instrumental in determining the dominant processes which control inertial particle settling. The first approach begins from the phase-space equation of the joint probability density function of the particles and will be the main approach we will discuss. This approach has the benefit of introducing no additional approximations other than the ones already found in the equations describing the motion of the dispersed and carrier phases (Bragg et al. 2021a). The second model is based off of a common eddy diffusivity approximation for the turbulent flux of particles found in the dry deposition literature (Hoppel 2002, 2005; Giardina and Buffa 2018; Farmer et al. 2021). This method has found practical and operational use but relies on a phenomenological closure scheme necessarily requiring empirical corrections. It is important to note that these methods take different approaches to estimate the same quantity; the average vertical particle velocity controlling the vertical flux.

In the following sections, we will show both the phase-space model and the phenomenological closure models, omitting some details for brevity and referring to external literature when reasonable.

3.1 Phase-Space Approach

The overall goal of this section is to highlight the steps in the derivation of a statistical model that predicts the vertical settling velocity taking into account the effects of particle inertia, gravity, and turbulence inhomogeneity. First, we begin by defining the joint PDF in position-velocity phase-space, $\mathcal{P}$, as:

$$\mathcal{P} = \langle \delta(\boldsymbol{x}_p - \boldsymbol{x})\delta(\boldsymbol{v}_p - \boldsymbol{v})\rangle, \tag{7}$$

where $\boldsymbol{x}_p$ and $\boldsymbol{v}_p$ are the time-dependent particle position and velocity relative to the origin, while $\boldsymbol{x}$ and $\boldsymbol{v}$ are the time-independent position and velocity coordinates of the phase-space in which the particle motion is being described. Here, $\delta(\cdot)$ is the Dirac delta function and $\langle\cdot\rangle$ denotes an ensemble average over all realizations of the system. Taking a time derivative of $\mathcal{P}$, we can form an evolution equation of the phase-space probability density for the particles:

$$\frac{\partial \mathcal{P}}{\partial t} + \nabla_{\boldsymbol{x}} \cdot (\langle \boldsymbol{v}\rangle_{\boldsymbol{x},\boldsymbol{v}}\mathcal{P}) + \nabla_{\boldsymbol{v}} \cdot (\langle \dot{\boldsymbol{v}}\rangle_{\boldsymbol{x},\boldsymbol{v}}\mathcal{P}) = 0, \tag{8}$$

where $\dot{\boldsymbol{v}}$ is the time derivative of the velocity, and $\langle\cdot\rangle_{\boldsymbol{x},\boldsymbol{v}}$ denotes an ensemble average conditioned on $\boldsymbol{x}_p(t) = \boldsymbol{x}, \boldsymbol{v}_p(t) = \boldsymbol{v}$. The operators $\nabla_{\boldsymbol{x}}$ and $\nabla_{\boldsymbol{v}}$ represent derivatives with respect position and velocity respectively. To obtain a governing equation for the number concentration of the particles, we can integrate the above equation over all velocities:

$$\frac{\partial \varrho}{\partial t} + \nabla_{\boldsymbol{x}} \cdot \left(\langle \boldsymbol{v}_p\rangle_{\boldsymbol{x}}\varrho\right) = 0, \tag{9}$$

where the particle number concentration is defined by:

$$\varrho(\boldsymbol{x}, t) = \int \mathcal{P} d\boldsymbol{v}, \tag{10}$$

and the particle mean momentum conditioned on $\boldsymbol{x}_p(t) = \boldsymbol{x}$ is defined by:

$$\varrho\langle \boldsymbol{v}_p\rangle_{\boldsymbol{x}} = \int \boldsymbol{v}\mathcal{P} d\boldsymbol{v}. \tag{11}$$

Equations (10) and (11) are consequences of the sifting property of the Dirac delta function. Thus, at steady state, the governing equation for the number concentration is:

$$\nabla_{\boldsymbol{x}} \cdot \left(\varrho\langle \boldsymbol{v}_p\rangle_{\boldsymbol{x}}\right) = 0. \tag{12}$$

By assuming a horizontally periodic domain, as we do in the simulations, the above equation simplifies to:

$$\frac{\partial}{\partial z}\left(\varrho\langle w_p\rangle_z\right) = 0, \tag{13}$$

where $\langle w_p\rangle_z$ is the average vertical component of the particle velocity conditioned on $z_p(t) = z$. Thus, we can compute the total vertical flux as the product of the number concentration and the average particle setting velocity as:

$$\varrho\langle w_p\rangle_z = F, \tag{14}$$

where F is the constant vertical number flux of the inertial particles, thereby giving us an algebraic relationship between the averaged vertical particle velocity, the total flux, and the horizontally averaged number concentration profile. Note that in practice, for the statistically stationary, horizontally homogeneous system we are considering, the conditional averages $\langle\cdot\rangle_z$ can be evaluated by spatial averaging over the homogeneous directions, as well as averaging in time.

At this point, we have not yet introduced a model for the average settling velocity, $\langle w_p\rangle_z$, in terms flow and particle properties. To do so, we form an evolution equation for the first moment of the joint PDF given by (11). This is done rigorously in previous work for particle momentum equations that contain hydrodynamic drag and gravity (see Skartlien 2007, Bragg et al. 2021a), so the exact algebraic details will be omitted here, and the result for a statistically stationary, horizontally homogeneous flow is:

$$\varrho\langle w_p\rangle_z = \varrho\langle u_p\rangle_z - \varrho v_g - \tau_p\varrho\frac{\partial}{\partial z}\left(\frac{1}{2}\langle w_p\rangle_z^2\right) - \tau_p\frac{\partial}{\partial z}\varrho S, \tag{15}$$

where $\langle u_p\rangle_z$ represents the average vertical fluid velocities sampled by particles at height $z_p(t) = z$, $v_g = \tau_p g$ is the Stokes settling velocity, and S represents the variance of the vertical particle velocity for particles at height $z_p(t) = z$. It is important to note that there are no additional approximations made in the derivation equation (15).

The above equation decomposes the mean particle momentum, $\varrho\langle w_p\rangle_z$, into contributions from various mechanisms, and the mechanisms contained in (15) are a consequence of the particle equations of motion, (3) and (4). Of interest in this work are the first and second terms on the right hand side (15): the contribution to the vertical flux associated with the average vertical fluid velocity sampled by the particles, and the Stokes settling velocity respectively, as it is expected that these terms dominate the vertical settling velocity sufficiently far away from boundaries.

The other terms, while important in certain cases, are not the main focus of this work, but will be touched on briefly here. The third term on the right hand side arises from the average wall normal convective acceleration of the particles, but was shown by Bragg et al. (2021a) to be negligible in the settling regime this work is concerned with. Finally, the fourth term on the right hand side is actually the sum of the contributions from two separate mechanisms. They are a diffusive flux arising from the partial decoupling of particle and fluid velocities and the turbophoretic drift velocity arising from vertical variation in the turbulence intensity. The magnitudes of these terms in a turbulent boundary layer are discussed at length in Bragg et al. (2021a). These terms are grouped together for notational simplicity as they are not the main focus of the paper.

As mentioned previously, the primary concern of this work is related to the estimate of the average settling velocity in the logarithmic region of a turbulent boundary layer (i.e. $z^+ > 100$). In this layer, the gradients of mean properties are relatively weak, so to leading order, we expect that for particles with low to moderate inertia, the dominant contribution to the vertical flux is associated with the fluid velocities sampled by the particles. However, for $\mathrm{St} \to 0$ (where St is a Stokes number based on an integral scale of the flow), we expect particles to exactly follow fluid streamlines, so particles become passive tracers. Likewise, in the limit of $\mathrm{St} \to \infty$, the particle trajectories are no longer correlated with the flow. Thus, in these limits and particles uniformly sample flow velocities.

Since $\langle u_p\rangle_z$ depends on both flow properties and particle properties, it is not known a priori, so it must be estimated. Bragg et al. (2012a) discusses several models in detail and their underlying assumptions. For this work, we use the following closure approximation for

the fluid velocity sampled by the particle (Reeks 1992):

$$\varrho\langle u_p\rangle_z = -\tau_p \frac{\partial}{\partial z}(\lambda\varrho) - \tau_p\gamma\varrho \tag{16}$$

where in the limit of a steady and horizontally homogeneous flow $\gamma(z)$ and $\lambda(z)$ (the functional dependence is suppressed in (16)) are functions that depend on the two-point, two-time correlations of the fluid velocity along particle trajectories:

$$\tau_p\lambda \;\; = \langle \Delta z u_p(z,t)\rangle, \tag{17}$$

$$\tau_p\gamma = -\langle \Delta z \tfrac{\partial u_p}{\partial z}(z,t)\rangle, \tag{18}$$

where the accumulated vertical displacement due to the fluid velocities sampled by the fluid over its path from a time t_1 to the measurement time t is written as:

$$\Delta z = \int_{t_1}^{t} u_p(z,t;s)\frac{1}{\tau_p}\left(1 - e^{(s-t)/\tau_p}\right) ds. \tag{19}$$

Equation (17) is interpreted as the correlation between changes in the vertical position of the particles and the velocities they sample along their trajectories, whereas (18) is the correlation between changes in the vertical position of the particles and the local fluid velocity gradients sampled along the particle trajectory. Bragg et al. (2012a) discusses how the different modeling approaches all have the form of (16) but differ in the details regarding how $\gamma(z)$ and $\lambda(z)$ are defined. These differences, while of interest from the perspective of mathematical rigor, are not important for the present study. As we will show in Sect. 4, γ plays an important role in balancing the gravitational accelerations (Skartlien 2007).

The utility of (16) as a representation of the average sampled velocities is that it effectively replaces the average fluid velocity sampled by the particle as a sum of two terms, one proportional to the concentration gradient (the second term on the right hand side), as is usual in phenomenological turbulence models, and a drift term that is proportional to the concentration itself, discussed below. This representation is useful in the limit of homogeneous turbulence in the absence of net particle sources or sinks and when the particles have been in the flow for long enough to reach a statistical equilibrium. In this case, the average particle concentration gradients (and diffusivity gradients) are necessarily zero, and only the drift term, γ, survives. This is because in such a flow, there would be no effect to break the translational symmetry of the system. In a boundary layer, the boundary itself breaks the translational symmetry, and so even in the quasi-homogeneous region of a boundary layer, the concentration gradient will not be identically zero. It can however be small because the flow is locally homogeneous, meaning that the translational symmetry breaking is coming from the far-field effect of the boundaries, not the near-field effect of local gradients in the flow. As discussed in Bragg et al. (2021a), this drift term captures the preferential sweeping mechanism (Maxey 1987; Wang and Stock 1993) that generates enhanced particle settling speeds even in homogeneous, isotropic turbulence, as observed in numerous studies such as Rosa et al. (2016) and Good et al. (2014). By comparison, a model that tries to represent $\varrho\langle u_p\rangle_z$ using only an eddy diffusivity closure (i.e. no drift term), such as that described in the next section, would never be able to represent the enhanced particle settling in the absence of gradients of the particle concentration, since the underlying assumption is that turbulent transport is driven by mean gradients. The closure presented in (16) attempts to capture such enhancement in this limit.

Justification for the above closure can be made based on several technical considerations. The underlying assumption is that the fluid velocities sampled by the particles form a random

process that is correlated in time. Generally speaking, for a non-Gaussian process, the statistics of the process are described by its infinite number of cumulants. This means that in the limit of a non-Gaussian process, the right hand side of Eq. (16) would have infinitely many terms, each corresponding to cumulants of different order (e.g. see the discussion in Reeks 1991). While the series may be asymptotic, computing all of the important contributions is not easy in practice, and the number of terms that should be retained in the series is not known a-priori. However, if the fluid velocities sampled by the particles form a Gaussian process, all cumulants are identically zero except those of second order, leaving behind only the terms written in (16) (Reeks 1991), thereby incurring no additional error. We will discuss this more in Sect. 4.

Note that in (16), the coefficient $\lambda(z)$ appears inside the derivative, so broadly speaking, (16) can be interpreted as a generalized eddy-diffusivity closure with an explicit drift component. Upon expanding the terms in the derivative, it becomes clear that we are representing the average sampled velocities as the sum of an eddy-diffusivity term with diffusivity $\tau_p\lambda(z)$, and a drift term:

$$\varrho\langle u_p\rangle_z = \underbrace{-\tau_p\lambda\frac{\partial\varrho}{\partial z}}_{\text{Diffusive term}} \underbrace{-\tau_p\left(\gamma+\frac{\partial\lambda}{\partial z}\right)\varrho}_{\text{Drift term}}, \tag{20}$$

As a brief summary, the equation which predicts the total enhanced settling velocity $\langle w_p\rangle_z$ (or alternatively the total vertical flux when multiplied by ϱ) is rewritten below in terms of the number concentration and its vertical gradient. To arrive at this equation, the decomposition of the sampled velocities, (20), was substituted into and (15), which gives the vertical number flux ($\varrho\langle w_p\rangle_z$) in terms of an advection–diffusion equation where the diffusivities and the drift coefficients are functions of λ, τ_p, S, and v_g:

$$\varrho\langle w_p\rangle_z = -(\underbrace{\tau_p\lambda}_{(1)}+\tau_p S)\frac{\partial\varrho}{\partial z} - v_g\overbrace{\left(1+\underbrace{\frac{\tau_p\gamma}{v_g}+\frac{\tau_p}{v_g}\frac{\partial\lambda}{\partial z}}_{(2)}+\frac{\tau_p}{v_g}\frac{\partial S}{\partial z}\right)}^{\text{Total correction}}\varrho. \tag{21}$$

We can see that writing the equation for the vertical flux in this way highlights the fact that the drift coefficient, γ, gradients of the variable diffusivity λ, and vertical particle velocity variance S, act as a correction to the Stokes settling velocity. Thus, the problem of modeling the vertical flux, $\varrho\langle w_p\rangle_z$, now comes down to computing ϱ, as well as the statistical correlations S, $\lambda(z)$, and $\gamma(z)$. For the work in this manuscript, we are concerned with only the λ and γ terms, since we will show that in several cases $S\partial_z\varrho$ is roughly balanced by $\varrho\partial_z S$ in the interior of the computational domain.

3.2 Estimating λ and γ

Our approach is to use the sampled velocities and concentration fields computed by the direct numerical simulations paired with a simple model for the diffusivity, λ, in order to compute a residual. We then argue that due to the statistical behaviour of the sampled velocities (discussed in the next section), the residual of the computed sampled velocities and the diffusive term is meaningful and corresponds to an added drift component, γ, that occurs because of preferential sweeping and turbulence inhomogeneity.

The simple model we will use for λ is given in Skartlien (2007), and arises by assuming that the turbulence is approximately locally homogeneous (Skartlien 2007; Zhang et al. 2023). Using this formulation, the diffusivity is computed as:

$$\tau_p \lambda = \langle w^2 \rangle \left(\frac{\tau_L^2}{\tau_p} \right) \frac{1}{1 + \frac{\tau_L}{\tau_p}}, \tag{22}$$

where $\langle w^2 \rangle$ is the mean squared vertical velocity of the flow and τ_L is the Lagrangian timescale of the turbulence (the time over which turbulent motions are correlated). There are corrections to this approach that include the influence of mean shear (see Skartlien 2007 for an example of a mean shear correction in homogeneous turbulence), but these terms can be ignored when considering horizontally homogeneous systems such as a turbulent boundary layer. To estimate τ_L, we use the model for an open channel turbulent boundary layer presented in Oesterlé and Zaichik (2004), which is:

$$\tau_L = -\frac{\kappa z}{u_\tau} \frac{\langle uw \rangle}{\langle w^2 \rangle}. \tag{23}$$

Both $\langle uw \rangle$ and $\langle w^2 \rangle$ can be estimated by appealing to standard wall models such as those presented in Smits et al. (2011), Kunkel and Marusic (2006), Marusic et al. (1997), but in our work, these qunatities are instead computed from the DNS data. For a simpler empirical fit to the data, one could alternatively use the model presented in Sikovsky (2019). It is also important to note that the definition of τ_L is dependent only on fluid properties, so in the one-way coupled limit, τ_L is not a function of the Stokes number or the settling velocity parameter. Thus, any effect on the particle transport by gravity is captured in the drift coefficient γ.

Strictly speaking, the correlation timescale over the Lagrangian particle trajectory, τ_{Lp}, which depends on height, the particle's Stokes number, and the settling velocity parameter, naturally occurs in the definition of λ. Common models for τ_{Lp} take inertia and the Stokes settling velocity into account independently, which are competing mechanisms in some regimes (Good et al. 2014). Berk and Coletti (2021) describes a model for τ_{Lp} that takes the particle Stokes settling into account, and is based on the crossing trajectories mechanism (Csanady 1963). Using their model, it can be shown that in the limit of a small Stokes settling velocity compared to the vertical root-mean-square velocity, the correlation time along the particle trajectory is identical to the Lagrangian correlation timescale at leading order with a correction proportional to $(\mathrm{Sv}^+)^2$. In the current work, the Stokes settling velocities are roughly an order of magnitude smaller than the root-mean-square velocity, meaning that τ_{Lp} is within 1% of τ_L. Thus, we approximate τ_{Lp} using τ_L for the purposes of computing λ.

Alternatively, Wang and Stock (1993) derive an empirical model for yet a different correlation timescale as a function of only particle inertia. Their model relies on the notion that at vanishing inertia, the correlation time along the particle trajectory is identically τ_L, while in the limit of large inertia, the timescale is the Eulerian integral timescale. Oesterlé and Zaichik (2004) comment that for an open channel turbulent boundary layer, the ratio of the Lagrangian and Eulerian integral timescales is roughly 0.8 at the channel centre, indicating that these timescales are roughly equivalent. Since the variation of the correlation timescale due to inertia does not vary significantly, we choose to use τ_L in (23). Furthermore, Bragg et al. (2012b) discusses the implications and associated errors by using τ_L instead of τ_{Lp} when modeling λ and γ in a synthetic boundary layer flow. They note that in spite of the errors associated with assuming $\tau_{Lp} \approx \tau_L$, estimates of γ and λ relative to equivalent particle tracking experiments are still better than those made assuming a passive scalar approximation

(which is equivalent to ignoring the drift term), and the magnitudes of those errors tend to decrease in the interior of their domain.

Finally, with an estimate for the diffusivity, λ, we can compute the residual between $\langle u_p \rangle_z$ and the diffusive term, which will be our estimate for the drift coefficient γ:

$$\tau_p \gamma = -\frac{\tau_p}{\varrho} \frac{\partial}{\partial z} \lambda \varrho - \langle u_p \rangle_z. \tag{24}$$

It should be noted that different expressions for γ exist, but they are written in terms of statistical correlations which can be hard to compute in practice (Bragg et al. 2012a; Reeks 2021). To our knowledge, no model for γ exists that can be written in terms of easily computed quantities in a turbulent boundary layer, as there is for λ.

3.3 Phenomenological Eddy-Diffusivity Approach

In large scale weather prediction models, as well as regional and global climate models, it is not feasible to represent the astronomical number of individual aerosols and particles in a Lagrangian frame of reference due to computational restrictions. Through there are hybrid methods to track Lagrangian parcels of air such as NOAA's HYSPLIT model, particles are often instead modelled as continua in an Eulerian framework and often represent a broad size class of particles, such as those less than 10 μm (called PM_{10}). This is an approach known as a bulk scheme (Jenkins et al. 2022). There are several other varieties such as sectional and modal schemes, and more information about these and their usage can be found in Kukkonen et al. (2012).

In these kinds of Eulerian frameworks, the concentration of various species follows an advection–diffusion equation according to mass conservation. In the following section, we provide the mathematical details for an interpretation of the enhanced vertical velocity by turbulence; one that makes several phenomenological assumptions about the impact of the turbulence. In the limit of horizontal homogeneity and stationarity, mass concentration obeys:

$$\frac{\partial}{\partial z} \left(-K(z) \frac{\partial C}{\partial z} - v_g C \right) = 0, \tag{25}$$

where the first term in the brackets comes from assuming that the turbulent flux of the tracer can represented by an eddy diffusivity closure, and the second term represents the flux associated with the Stokes settling velocity. Integrating this equation with respect to height, we arrive at the following:

$$-K(z) \frac{\partial C}{\partial z} - v_g C = F, \tag{26}$$

where F represents the net mass flux which is constant with height.

The equation can be solved to reveal:

$$F + v_g C(z) = \left(F + v_g C_0 \right) e^{-v_g R}, \tag{27}$$

where C_0 is a reference concentration at a height δ_0, and R is interpreted as a resistance to transport:

$$R = \int_{\delta}^{z} \frac{dz'}{K(z')}, \tag{28}$$

which has dimensions of time over length. As an example, to recover the familiar Rouse profile (Rouse 1937), the turbulent flux is assumed to exactly balance the flux due to Stokes

settling, implying $F = 0$, and the tracer is assumed to respond instantaneously to the eddy velocities (i.e. in the limit of vanishing inertia). This allows us to use the familiar log-layer assumption for the eddy diffusivity $K(z) = \kappa u_\tau z$ (assuming a turbulent Schmidt number of one), where κ is the Von Karman constant.

For net deposition conditions, $F < 0$ but is constant with height. Understanding that we can write $F = -v_d(z)C(z)$, where v_d is known as the deposition velocity at height z, we recover:

$$v_d = \frac{v_g \left(1 - \frac{C_0}{C(z)} e^{-v_g R}\right)}{1 - e^{-v_g R}}. \tag{29}$$

Note that v_d and $\langle w_p \rangle_z$ actually correspond to the same quantity; the average vertical velocity of the particles. However, different notation is intentionally chosen so as to differentiate between the phenomenological model for the the average vertical velocity of the particles, which we call v_d, and the phase space model for this quantity, which we denote by $\langle w_p \rangle_z$.

A consequential assumption of the above model is that the turbulent flux of particles is represented by the eddy-diffusivity closure:

$$\langle cw \rangle \approx -K(z) \frac{\partial C}{\partial z}, \tag{30}$$

where c is the fluctuating particle concentration. From the discussion in the previous section, we know that the flux of particles by the sampled turbulent velocities should actually be governed by the sum of a drift term proportional to the concentration, as well as a term proportional to gradient of the concentration (for low and moderate Stokes number). Thus, the closure shown in (30) is a phenomenological assumption.

Another assumption comes from the representation of the diffusivity $K(z)$ itself, and by extension, R. R is typically parameterized in terms of how different mechanisms in the lower atmosphere affect the collection efficiency of inertial particles (Emerson et al. 2020). These collection efficiencies are functions of the land use category in question. Several examples include forest canopies, deserts, tundras, open water, and fields (Farmer et al. 2021). The primary purpose of this paper is not to modify existing parameterizations of the resistance, but to comment on how a phenomenological model compares to that of a first principles model. To that end, we use a form of the resistance which includes only the effects of turbulence and inertia. In its simplest form, we write the normalized resistance as a sum of the aerodynamic resistance and what is known as the surface resistance (Zhang 2001) (ignoring Brownian diffusion and interception, more on this below):

$$u_\tau R = u_\tau R_a + u_\tau \left(\frac{\mathrm{St}^+}{\alpha + \mathrm{St}^+}\right)^{-\beta}, \tag{31}$$

where R_a is known as the aerodynamic resistance and takes the form:

$$R_a = \frac{1}{\kappa u_\tau} \log\left(\frac{z}{\delta_0}\right), \tag{32}$$

where α and β are positive constants that depend on the land use category (Zhang 2001), δ_0 is taken to be the maximum height of the buffer layer, and z is the height at which the deposition velocity is to be calculated. In this simplified model, the second term on the right hand side of (31) parameterizes the impact of inertia on the resistance. It is important to note that in operational models, there are other terms that should be included in (31). For example, it is known that Brownian diffusion affects the deposition of particles of various

sizes (Seinfeld and Pandis 1998; Emerson et al. 2020) for land use types without collectors (such as leaves, trees, grass). However, deposition enhancement by Brownian diffusion is only significant for particles much smaller than 0.1 μm, which translates to $St^+ < 10^{-4}$ for our DNS so it is ignored for simplicity. Furthermore, for surfaces which have collectors, their impact on the deposition must be taken into account in operational models, and this is done through a process known as interception. It turns out that the contribution to the total deposition velocity by interception is much smaller in magnitude than both the contribution by impaction and by the Stokes settling velocity anyways (Farmer et al. 2021), and is therefore ignored in (31). Thus, the simplest model to which we can compare DNS results to is simply to include a model for impaction (i.e. the second term on the right hand side of (31)). In the limit of $St^+ \to 0$, the second term above takes a form proportional to $(St^+)^{-\beta}$ indicating that $R \to \infty$. In this limit, the model shown in (29) says that $v_d \to v_g$ which is what is expected in the limit of small St^+. In the limit of $St^+ \to \infty$, the overall resistance at a height z approaches a constant value. According to (29), since v_g is coupled to St^+ through the constancy of g, this implies that again $v_d \to v_g$, which is the correct relationship in the ballistic limit.

Note that (29) is implicitly a function of the local concentration. In order to estimate the deposition velocity from (33), we will assume that $C(z) \gg C_0$ (i.e. we are assuming that the second term in the numerator of (29) is negligible compared to unity):

$$v_d = \frac{v_g}{1 - e^{-v_g R}}. \tag{33}$$

This is not strictly necessary, but as $C_0/C(z)$ approaches zero, this implies that the concentration at the measuring height z is much larger than the reference concentration, the second term in the numerator of (29) becomes small compared to unity. Mathematically speaking, this limit corresponds to the maximum enhancement predicted by the phenomenological model. On the other hand, as $C(z) \to C_0$, the implication is that the concentration at a measurement height z is nearly identical to the reference concentration. If this is the case everywhere across the turbulent boundary layer, then there is no vertical variation in the concentration profile, and mathematically, v_d tends back to v_g, the Stokes settling velocity. This result is consistent within the context of this model, as the gradient-diffusion closure implicitly assumes that all turbulent transport must be a consequence of gradients of the mean concentration. Of course this is certainly not true of real turbulent flows, e.g., homogeneous isotropic turbulence, where enhancement is seen when the mean concentration is constant (Maxey 1987; Wang and Maxey 1993).

As a final point, in this work, we will use "settling velocity" and "deposition velocity" interchangeably, but in an effort to discriminate between the two approaches discussed in the following results, we will use $\langle w_p \rangle_z$ when referring to the settling velocity computed from the DNS and when referring to the phase-space approach, and we will use v_d when discussing the deposition velocity associated with the phenomenological modeling approach. Furthermore, since the particles do not change their radius over the course of the simulation, the number concentration, denoted by ϱ, is linearly related to the mass concentration, denoted by C. Therefore, the number flux is also linearly related to the mass flux.

In summary, we estimate the settling velocity enhancement of inertial particles by turbulence using two different methods. The first is based on an evolution equation for the particle phase-space PDF from which we can derive an exact equation predicting the average particle settling velocity. This equation includes two unknown terms, and we place our focus on estimating one of them; the average sampled turbulent velocities. We expect this term to be the main contributor to the enhanced settling velocities in interior of a turbulent boundary

layer. Under the assumption that the turbulent velocities sampled along a particle trajectory form a Gaussian random process, we can write the average sampled velocities as a sum of a diffusion term and drift term. By assuming low to moderate St^+ and low v_g/w_{rms} and that the turbulence is locally homogeneous, we can use a closed form expression for the diffusion term in conjunction with DNS data to estimate the relative importance of the drift term.

Alternatively, the second model we consider is based on a phenomenological closure assumption which parameterizes the turbulent transport as a diffusive process only. This model makes use of a turbulent eddy diffusivity which is parameterized in terms of empirical models of the aerodynamic and inertial resistance, calibrated to observations over different land use categories.

4 Results

4.1 Settling velocity enhancement for Numerical Experiment 1

We will begin the analysis and comparison by briefly highlighting the main characteristics of the flow statistics and the cases in Numerical Experiment 1 (shown in Table 1). Figure 2a shows the mean horizontal velocity profile for $\mathrm{Re}_\tau = 630$, Fig. 2b shows the components of the velocity variance and the vertical momentum flux, and finally Fig. 2c shows the Lagrangian correlation timescale as a function of the vertical coordinate. We can see that the DNS reproduces the theoretical laminar sub-layer and log layer scalings, and the velocity variances and vertical momentum flux are in good agreement with past work on turbulent open channel flows at similar Reynolds number (Marchioli et al. 2008). Furthermore, the Lagrangian correlation timescale tends to take on a nearly constant value over the laminar sub-layer, and begins to increase as a function of the vertical coordinate for roughly $z^+ > 100$.

Figure 3a–c show the DNS-computed settling velocity (dashed curves), the sum of the average sampled velocities and the Stokes settling velocity (solid curves) and the sum of the diffusive flux and turbophoretic terms (dot-dashed curves) for $\mathrm{St}^+ = 0.1$, 10 and 100 respectively and for all three values of Sv^+ for each. The third term on the right hand side of (15) has been omitted as it is known to be negligible. First, we will focus on the cases with $\mathrm{St}^+ = 10$, Fig. 3b, as it clearly shows the role of each settling mechanism. We can identify that the overall settling enhancement relative to the Stokes settling velocity decreases as

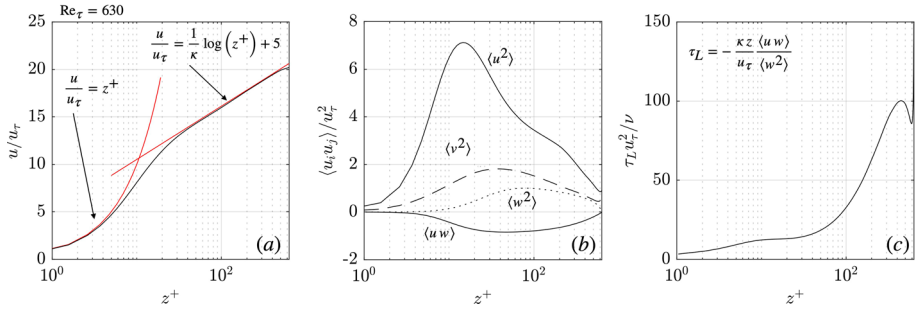

Fig. 2 Panel **a** shows the mean horizontal velocity profile computed from the DNS overlaid with the theoretical viscous sub-layer and log layer profiles. Panel **b** shows the components of velocity variance and the vertical momentum flux normalized by u_τ^2. Panel **c** shows the Lagrangian correlation timescale, equation (23) highlighting its increasing nature in the log layer

Sv^+ is increased. Within the interior of the domain, (about $100 < z^+ < 500$) the grouped diffusive flux and the turbophoretic drift terms are negligible for all cases except the case with the lowest Sv^+, which begins to increase with height implying an upward tendency, though it is weak. Though these terms are implicitly dependent on the particle velocities (and thus Sv^+), they are explicitly dependent on St^+, so by increasing Sv^+, the relative contribution in the boundary layer decreases. Therefore, we can see that the decreased turbulent settling velocity must come from the reduction in the difference between the sampled velocities and the Stokes settling velocities as Sv^+ is increased.

For $St^+ = 0.1$, Fig. 3a, the settling velocity in the interior is well approximated by the sum of the Stokes settling velocity and the average velocity sampled by the particles, as this was the dominant balance at low Stokes number, pointed out by Bragg et al. (2021a) since all other terms in (15) are proportional to St^+. By comparison, adequate representation of the average settling velocity for $St^+ = 100$, Fig. 3c, requires the inclusion of all terms in (15) (aside from the term including $\langle w_p \rangle^2$). Thus, to fully model the settling velocity at $St^+ = 100$ at the current Re_τ, a separate model of the diffusive flux and the turbophoretic drift term (or equivalently of the turbophoresis and the particle fluctuating covariance tensor) is required. Since the goal of this work is to compare models of the sampled velocities ($\langle u_p \rangle_z$), we will not comment on models of these quantities, but refer the reader to Zhang et al. (2023) for a detailed discussion. These profiles imply that the traditional view of preferential sweeping from Wang and Maxey (1993) is modified as Sv^+ is varied independently from St^+, which is also discussed and highlighted in Good et al. (2014). The modification to the traditional picture of preferential sweeping for a given St^+ due to Sv^+ is demonstrated conceptually in Fig. 4.

As a settling inertial particle approaches an eddy, the particle is preferentially swept to the downward side of the eddy, meaning that inertial particles will preferentially sample negative velocities. For a fixed St^+, increasing Sv^+ implies an increase in the Stokes settling velocity. This means that in one relaxation timescale, a particle travels a distance (normalized by wall units) $\delta \approx g\tau_p^2 u_\tau/\nu$. This distance is only approximate because the speed at which the particle enters a given eddy is actually a function of its history, as it was presumably accelerated by eddies that it had previously encountered. Thus, for a fixed St^+, increasing Sv^+ allows the inertial particle to penetrate deeper into a given eddy before it can relax to the local flow conditions. Though the exact form of a turbulent eddy is not known, models (Pullin

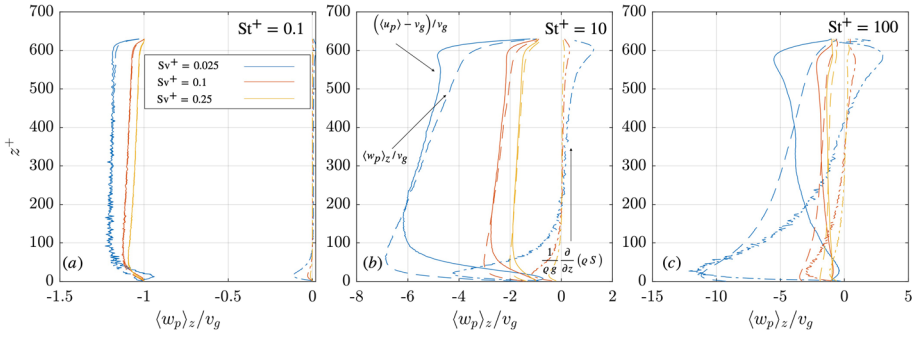

Fig. 3 Profiles of the averaged settling velocity (dashed curves), the averaged fluid velocity sampled by the particle (solid curves), and the averaged diffusive flux and turbophoretic drift terms (dot-dashed curves) for $St^+ = 0.1$, 10, and 100 in panels **a**–**c** respectively. Information for the cases shown can be found in Table 1. Recall that the diffusive flux and the turbophoretic drift terms are grouped together

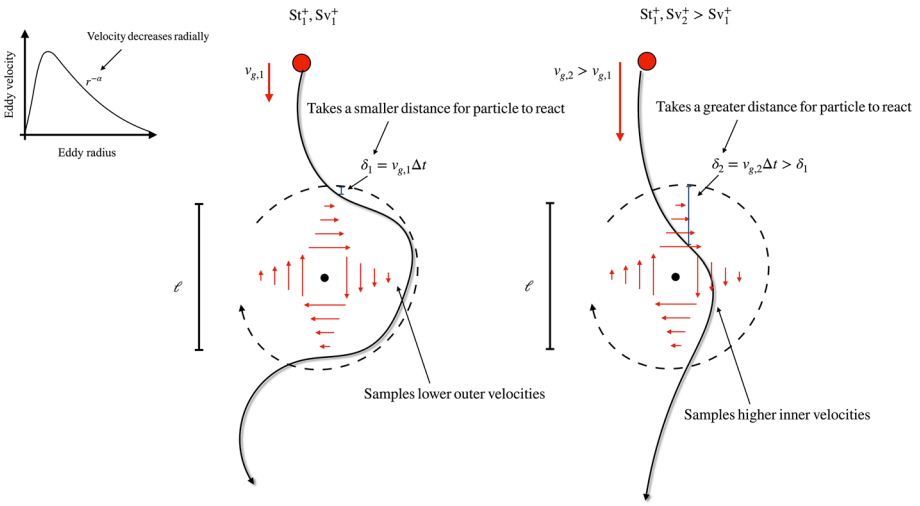

Fig. 4 The modification of preferential sweeping due to the variation in Sv^+ at constant St^+. The top left corner is a prototypical relationship between the velocity of a turbulent eddy and the radial distance away from its center. The middle and rightmost panel show a turbulent eddy of size ℓ (outline by the dashed curve), and the qualitative velocity distribution denoted by red arrows within. The particle (the red circle) follows the trajectory denoted by the solid curved arrow. For a given low to moderate Stokes number and Sv^+, the particle penetrates a certain distance into the eddy before as it relaxes to the local velocity field. It is then swept to the downward side of the eddy. If Sv^+ is increased (or alternatively g), then the particle penetrates further into the eddy as it is settling at a higher rate. Therefore, it samples larger inner velocities

and Saffman 1998) point to turbulent eddies having velocity distributions that are inversely proportional to the distance from the eddy core. Thus, a particle penetrating further into a turbulent eddy samples higher velocities before it is relaxes to the local fluid velocity. This means that, on average, particles at a given Stokes number sample higher velocities at higher Sv^+. This picture is true until the St^+ is large enough that the particle trajectory becomes uncorrelated from the fluid motion regardless of δ.

Particle-turbulence interactions in a real turbulent flow are of course much more complex than those in this simple cartoon. Nevertheless, it provides some insights into how the sampling of the flow by the particles could increase with increasing Sv^+ for a given St^+. It cannot be true in general, however, because for $\mathrm{Sv}^+ \to \infty$ the particles settle ballistically through the eddies and there is no preferential sweeping.

4.2 Modeling the Fluid Velocity Sampled by the Particle

In the following sections, we use a combination of the DNS data and the model in (22) to estimate the magnitudes of the terms in (16) as well as their behaviour with respect to St^+ and Sv^+. Recall that the base assumption regarding the applicability of (16) is that the vertical component of the sampled velocities are normally distributed about their mean value (Skartlien 2007). In Fig. 5, we use the skewness and kurtosis of the distributions of sampled velocities to assess their statistical behaviour with height. To compute these quantities with height, we break the domain into slabs of thickness $z^+ = 10$, and for all particles within a given slab, we compute the skewness (dashed curves) and kurtosis (solid curves) of distributions of sampled velocities. We have also denoted the skewness (zero) and

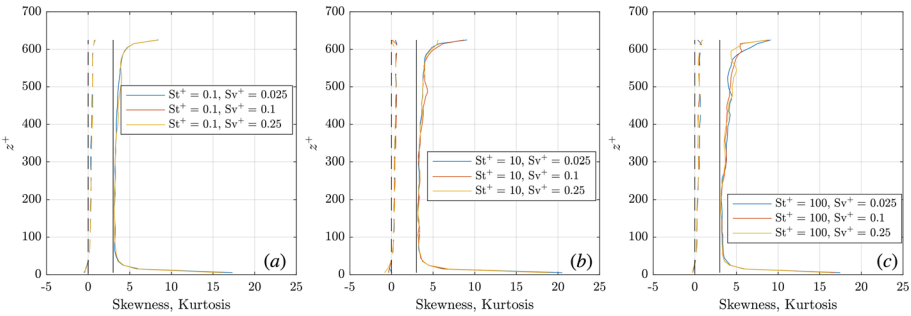

Fig. 5 Profiles of the skewness and kurtosis of sampled velocities in slabs of thickness $z^+ = 10$, for $St^+ = 0.1$ in panel **a**, $St^+ = 10$ in panel **b**, and $St^+ = 100$ in panel **c**. Each curve color corresponds to each value of Sv^+. Dashed black line is zero skewness, and the solid black line is a kurtosis of 3

kurtosis (three) of a normal distribution with the dashed and solid black lines respectively for comparison.

We can see that for all cases, the kurtosis of the distributions vary significantly near the upper and lower boundaries, but the actual values depend relatively weakly on St^+ and Sv^+. This indicates that the non-Gaussianity of the velocities sampled by the particles is mainly due to non-Gaussianity of the underlying fluid velocity field, rather than being due to a biased sampling of the velocity field due to particle inertia. The PDFs (not shown) indicate that the deviations of the kurtosis from the value for a Gaussian distribution are both due to the sampled velocities exhibiting an enhanced probability of low and high values relative to those for a Gaussian PDF, i.e. the PDF of the sampled velocities are more peaked around zero and have heavier tails than a Gaussian PDF. Nevertheless, within the interior of the domain, the statistics are close to those of a normal distribution, though they are slightly positively skewed and are slightly leptokurtic. Furthermore, it is clear that there is variation in the statistics with height within the interior with increasing St^+ and Sv^+, but these differences are relatively small, especially compared to those near the boundaries. Thus, using these plots, we arrive at the conclusion that within the interior of the domain, say $100 < z^+ < 500$, the interpretation that the residual in Eq. (24) represents the drift coefficient is justified. Comparatively, since the distributions are strongly leptokurtic within several wall units of the lower and upper boundaries, Eq. (24) cannot be interpreted as a the drift coefficient in these regions.

Next, using the DNS data, we can calculate τ_L using (23) to determine both the integral Stokes number, St, as well as the diffusivity, $\tau_p \lambda$ (i.e. there is no need for the residual in (22)). These quantities are shown in Fig. 6a and b respectively. We can see that across the interior of the domain (say in the range $100 < z^+ < 500$), the range of the integral Stokes number for a given St^+ is less than an order of magnitude. Recall that since τ_L is only a function of fluid properties, cases with fixed St^+ and different Sv^+ will have the same integral Stokes number. Furthermore, we can see that by increasing St^+ by a factor of 10 or 100, we also increase St at a given height by a factor of 10 or 100.

Note that for small and moderate St^+ (0.1 or 10), the integral Stokes number is less than unity across the entire interior of the domain, suggesting only a weak decoupling of the particle trajectories from the Lagrangian fluid trajectories there. This correlates with the fact that the within the interior, distributions of sampled velocities are approximately Gaussian (see Fig. 5a, b), so we should expect the closure discussed in (16) to be approximately valid for these cases. For $St^+ = 100$, the integral Stokes number varies from about one near the midpoint of the domain to five near the viscous sublayer, and this is connected to the stronger

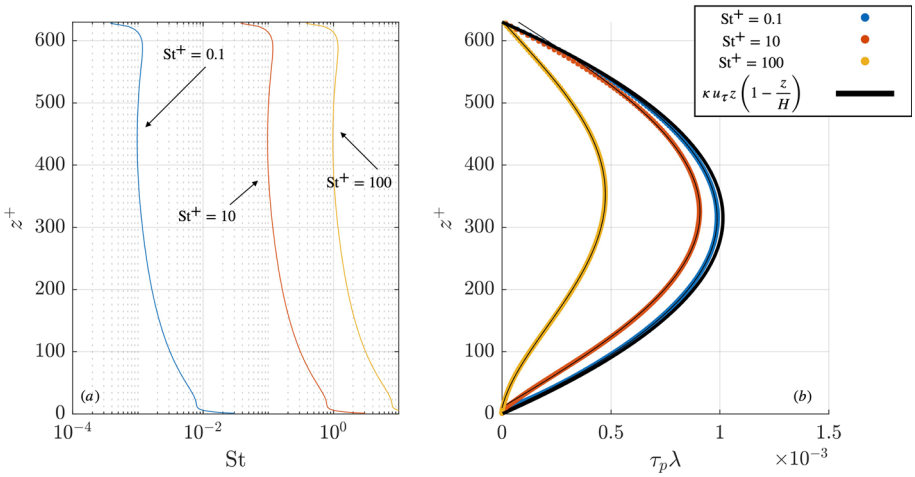

Fig. 6 Panel **a** shows the integral Stokes number for $St^+ = 0.1$, 10, and 100 and panel **b** shows the computed $\tau_p\lambda$ for each St^+ with $Sv^+ = 0.1$. (dots), and a fourth order polynomial fit to each dataset (thin black line) and the quadratic diffusivity profile using a log layer scaling from Hoppel (2005) (thick black line)

non-Gaussianity of the sampled velocities for this value of St^+. Indeed, even in the context of isotropic turbulence, the statistical properties of the flow sampled by the particles is a strong function of the particle inertia, with moderately inertial particles avoiding the most extreme fluctuations in the flow, while weakly and strongly inertial particles sample the flow more uniformly (Ireland et al. 2016).

Given our model for τ_L, we can now use $\langle w^2 \rangle$ to compute $\tau_p\lambda$, which can be interpreted as the diffusivity for the "gradient" based part of the closure. Shown in 6b are values of $\tau_p\lambda$ computed by the DNS for all cases at $Sv^+ = 0.1$ in Numerical Experiment 1, and these are plotted as circular markers. A fourth order polynomial fit in the region $40 < z^+ < 600$ is overlaid on the data. This interval was chosen to avoid non-physical boundary effects. Recall that since λ is only a function of fluid properties (τ_L and $\langle w^2 \rangle$), as well as the relaxation timescale (τ_p), changes in Sv^+ due to changes in g will not change the profile of λ.

The choice to use a fourth order model is arbitrary, but qualitatively speaking, other common forms of the scalar and momentum diffusivities in phenomenological closures often take similar even order polynomial forms. For example, for a neutrally stratified turbulent boundary layer with a logarithmic mean velocity profile, a quadratic model for the momentum diffusivity can be easily derived to be $K_q(z) = \kappa u_\tau z \left(1 - \frac{z}{H}\right)$ (Fischer 1973; Hoppel 2005). This profile is plotted on Fig. 6b as a thick black curve. Furthermore, for an unstable planetary boundary layer, scalar diffusivities are often represented by polynomials of fractional order in the vertical coordinate (Holtslag and Moeng 1991; Wyngaard and Brost 1984), and a similar approach was taken by Nissanka et al. (2018) who used a blend of linear and cubic scalar diffusivity profiles to model particle dispersion within the marine atmospheric boundary layer. Often, for the bottom 100 m of the ABL, it is common to take a diffusivity which is linear in height (see Kantha and Clayson 2000 for example).

We can see from Fig. 6b that $\tau_p\lambda$ for $St^+ = 0.1$ approaches the diffusivity profile predicted by a quadratic log layer scaling discussed above. This is a consequence of the particles acting as passive scalars in the low St^+ limit. It is known in that in this limit, the drift coefficient

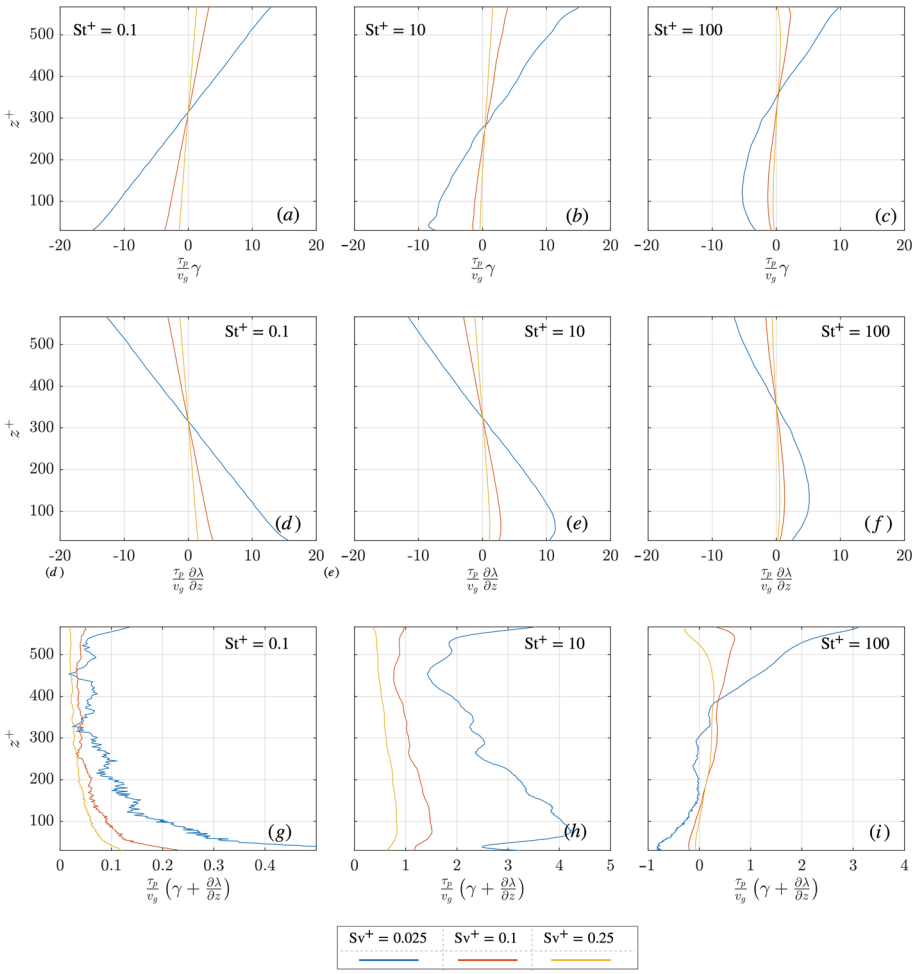

Fig. 7 A comparison of the magnitude of terms that make up the drift coefficient. Profiles of $\tau_p \gamma / v_g$ are presented in panels **a**–**c** and profiles of $\frac{\tau_p}{v_g}\frac{\partial \lambda}{\partial z}$ are presented in panels **d**–**f**, and their sums are presented in panels **g**–**i**. Each curve within a panel corresponds to a different Sv^+, while each column corresponds to a different St^+

takes the form:

$$\gamma = -\frac{\partial \lambda}{\partial z}, \tag{34}$$

thus (16) only contains the gradient diffusion term. This is known as the passive scalar approximation (Bragg et al. 2012b). Further increasing St^+ to 10 or 100, we decrease the diffusivity relative to the theoretical functional form. According to (17) (the definition of λ), this must come from the fact that the vertical displacements of the particles associated with the sampled velocities become smaller.

Using the estimate for $\tau_p \lambda$ from Fig. 6b, the known number concentration ϱ, and averaged sampled velocities $\langle u_p \rangle_z$ from the DNS, we can estimate the residual from Eq. (24) to help us to understand what γ ought to be for Eq. (16) to adequately represent the sampled velocities.

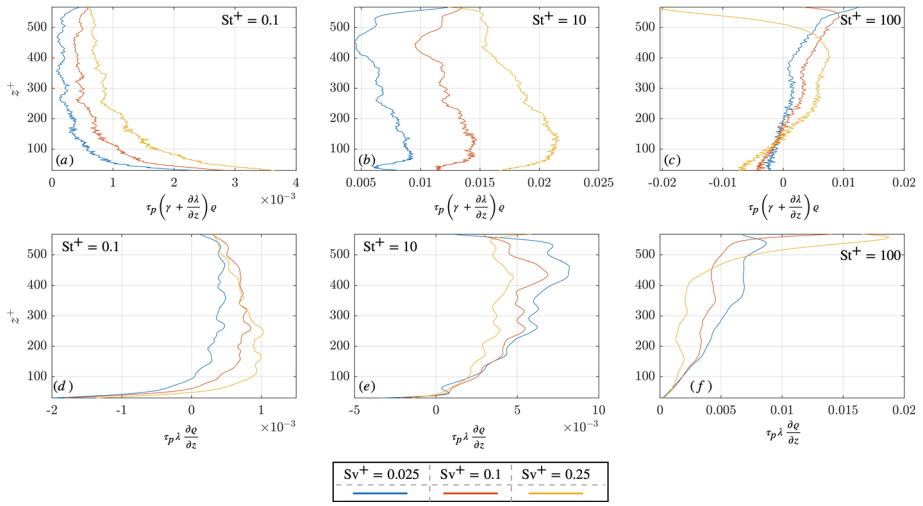

Fig. 8 Profiles of the drift component of (20) are presented in panels **a**–**c** and profiles of the diffusive component of (20) are presented in panels **d**–**f**. Each curve within a panel corresponds to a different Sv^+, while each column corresponds to a different St^+. Data smoothing has been applied to the concentration profiles to in order to smooth the derivatives

Furthermore, we can compare this to $\frac{\partial \lambda}{\partial z}$ to identify the dominant contribution to the drift term. These quantities are plotted in Fig. 7.

By virtue of the the fact that τ_L is a fluid property, the definition of λ we use in this work is not a function of Sv^+. Thus, dependence on Sv^+ should be encapsulated within the residual in (24), γ. Profiles of $\tau_p \gamma / v_g$ for each St^+ are shown in Fig. 7a–c, while profiles of $\frac{\tau_p}{v_g}\frac{\partial \lambda}{\partial z}$ are shown in Fig. 7d–f, and profiles of their sums are shown in Fig. 7g–i. We can see that for $\mathrm{St}^+ = 0.1$, the terms in the drift component nearly cancel eachother out (in Fig. 7a, d), leading to relatively small changes to the Stokes settling velocity in Fig. 7g. These results are consistent with the passive scalar approximation discussed earlier (equation (34)), which is appropriate in the limit $\mathrm{St} \to 0$. By increasing St^+ to 10 in Fig. 7b, e, and h, the dependence of $\tau_p \gamma$ on Sv^+ within the interior is much stronger. The result is that the enhancement of the Stokes settling velocity due to the drift is increased by 200-400% for $\mathrm{Sv}^+ = 0.025$ and roughly 100% for $\mathrm{Sv}^+ = 0.25$, shown in Fig. 7h. This means that to adequately model enhanced settling, inclusion of the drift coefficient γ as well as its dependence on Sv^+ in a model is imperative, especially for moderate Stokes number. Lastly, we can see that the behaviour of the γ profiles becomes more complex for $\mathrm{St}^+ = 100$, shown in Fig. 7c, f, and i. Specifically, we can see that in the range $z^+ < 200$, where we know that the kurtosis of the distributions are close to three (see Fig. 5c), the total drift coefficient is actually negative, indicating that in this region, the effective Stokes settling velocity (i.e. the total drift contribution on the right hand side of (21) associated with γ and λ) is actually reduced, and this effect tends to decrease with increasing Sv^+.

Next, with detailed information about λ and γ in hand, we plot the components of the total flux that are due only to the sampled velocities and the Stokes settling velocity, i.e. Equation (21) but only including to terms highlighted by the under braces. The drift components are shown in Fig. 8a–c and the diffusion components are shown in Fig. 8d–f. Each column corresponds to a value of St^+ while each curve corresponds to a specific value of Sv^+.

The primary finding here is that the drift contribution implied by the DNS is in fact up to an order of magnitude more important than the diffusion component (ignoring the terms including S in (21)) for moderate St^+ and high Sv^+, shown in Fig. 8b and e, and this must come from the enhancement by preferential sweeping. This difference decreases as Sv^+ is decreased since the diffusion component tends to increase in magnitude overall, probably due to the crossing trajectory effect, while the drift coefficient decreases in magnitude overall. It is sensible for the drift coefficient to decrease in magnitude in the limit of $\mathrm{Sv}^+ \to 0$ since in this limit, there is no net downward flux and on average particles begin to sample upward motions as frequently as downward motions within the interior. On the other hand, for both high and low St^+, the drift component and the diffusion components are at least comparable in magnitude within the interior of the domain.

Roughly speaking, we can see that as the Stokes number increases, the magnitude of the diffusive profiles within the interior for all Sv^+ increases by a factor of 3 to 10 (depending on Sv^+) between $\mathrm{St}^+ = 0.1$ and 10, while the differences between the diffusive profiles for $\mathrm{St}^+ = 10$ and $\mathrm{St}^+ = 100$ are not nearly as large. On the other hand, the overall magnitude of the drift coefficient reaches a peak at the moderate Stokes number. It is interesting to note that in Fig. 8d, the diffusion for the $\mathrm{Sv}^+ = 0.025$ case actually has the lowest magnitude and the lowest drift, implying that the averaged sampled velocities begin to approach zero in the passive scalar limit.

These results indicate that an understanding of the parametric behaviour of the drift correction is imperative for adequate representation of the fluid velocities sampled by the particle in the log layer for low and moderate Stokes number. These are important observations since for phenomenological modeling efforts, the entirety of the turbulent flux is assumed to be encoded in an eddy diffusivity closure, but it is clear that in the moderate St^+ limit, the majority of the settling velocity enhancement actually comes from the drift component, and the magnitude and structure of the drift strongly depends on both St^+ and Sv^+. We discuss these implications next.

4.3 Deposition Velocity According to the Phenomenological Approach

Prior to the usage of the closure for the sampled vertical fluid velocities in (16), the phase-space approach outlined in Sect 3.2 is exact, in the sense that it introduces no additional assumptions about either the particle or fluid dynamics aside from those already in the equations of motion themselves (Bragg et al. 2021a). However, it is very general and identifying opportunities for modeling simplification can be quite challenging for weather and dispersion applications. Therefore, it is useful to discuss the results from the DNS data in terms of a phenomenological model which is similar to an approach used ubiquitously throughout the atmospheric deposition literature. As a reminder, the phenomenological model interprets all turbulent transport as purely diffusive, and ignores any potential drift component.

In this section, our goal is to compare the DNS data from the cases highlighted in Table 2 (Numerical Experiment 2) with the phenomenological model presented in Eq. (33). First, Fig. 9a shows the settling velocity enhancement for Numerical Experiment 1 (Γ is varied) as filled markers, and the settling velocity enhancement of Numerical Experiment 2 (two values of constant Γ) as asterisk markers, all evaluated at a height of $z^+ = 180$. The common behaviour is that there is a maximum in the settling enhancement somewhere in the neighborhood of $\mathrm{St}^+ = 10$ (St in the range of 0.1 to 1 according to Fig. 6) for all cases, which qualitatively agrees with past studies on the settling velocity enhancement of inertial particles (Wang and Maxey 1993; Rosa et al. 2016). However, for cases at constant Γ (Numer-

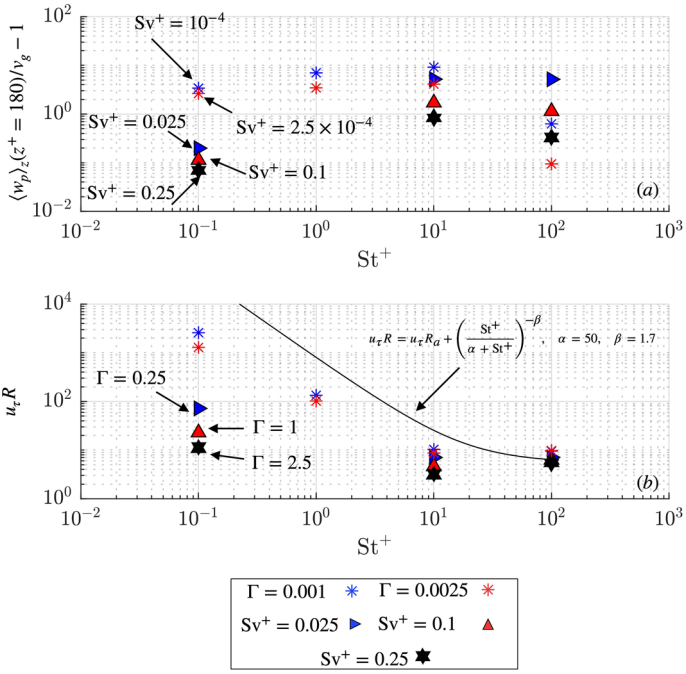

Fig. 9 The settling velocity enhancement plotted against St^+ at $z^+ = 180$, panel **a**, and the normalized resistance computed from the DNS plotted against St^+ at $z^+ = 180$, panel **b**. Data from cases in Table 1 are plotted as filled markers. Data from cases in table 2 are plotted as stars. The resistance model from Zhang (2001) with $\alpha = 50$ and $\beta = 1.7$ is included on panel **b**

ical Experiment 2; asterisks), the enhancement is sustained at very low St^+, suggesting that the velocities sampled by the particles tend to become more important in determining the enhancement at such low Sv^+. It has been shown previously in a turbulent channel flow that for Sv^+ in the neighborhood of 10^{-3} or 10^{-4}, that the magnitude of Sv^+ does not play a significant role in the dynamics of the particles outside a very small region near the bottom boundary (Bragg et al. 2021b), so the dominant effect leading to settling enhancement is the preferential sweeping by turbulent eddies. In these cases, distributions of the sampled velocities tend to converge around the same value when normalized by the Stokes settling velocity (not shown).

Figure 9b shows the resistance, R, back calculated using (33) assuming that $v_d = \langle w_p \rangle_z$ for all cases in numerical experiments 1 and 2 as well as the theoretical curve from Zhang (2001) using $\alpha = 50$ and $\beta = 1.7$. We can see that as Γ becomes smaller (denoted by cases marked with asterisks), the data begins to approach this empirical curve in the low St^+ range, whereas when Γ becomes large (denoted by cases marked with solid markers), it is clear that the data diverges from empirical curve in this same range. Different models for the inertial resistance such as those from Slinn and Slinn (1980), Giorgi (1986), Zhang (2001), Emerson et al. (2020) will change the slope of this curve in the low St^+ range, but as far as we are aware, none of these models attempt to define the variation in slope as a function of Γ, even though we have demonstrated that it matters. Furthermore, as the Stokes number increases, the data points tend to group together and approach the asymptotic aerodynamic resistance component. In the model from Hoppel (2005), this corresponds to the resistance acquiring a

constant value, leading to negligible velocity enhancement as St^+ increases, which our DNS qualitatively agrees with.

An important point to mention is that the empirically determined constants which characterize the aerodynamic resistance (α and β) were calibrated to data measured under Earth-like conditions. Thus, the resistance parameterization is expected to accurately model conditions which are relevant to that environment. For example, under normal neutral atmospheric boundary layer conditions on earth, we expect u_τ to take values in the neighborhood of 10 cm/s to 1 m/s (see Vickers et al. 2015 for example), and since g and ν are roughly constant, Γ takes on values between 10^{-4} and 10^{-1}. This observation may explain why when Γ is close to this estimated range, the data tends to approach the empirical curve, while for Γ out of this range, the data appears to diverge from this relationship. This observation also means that we should not necessarily expect the empirical curve to match the DNS data quantitatively for the experiments in Table 1, or more generally, environments where Γ significantly diverges from the geophysically relevant range. Consequently, by over-estimating the resistance, $u_\tau R$, we under-estimate the overall deposition velocity for low and moderate Stokes number.

Furthermore, if we interpret impact of the turbulence on the vertical transport as having a drift component in addition to the a diffusion component, as we have in Sect. 4.2, then the empirically determined constants could be inadvertently compensating for a mechanism that is specifically ignored in the phenomenological interpretation. In an effort to demonstrate the effect of ignoring the drift component in the phenomenological interpretation, we have compared the re-scaled cases from Numerical Experiment 2 (shown in Table 2) to the theoretical deposition velocity after solving (33), shown in Fig. 10. To re-scale these cases, we found an equivalent friction velocity implied by our choice of Γ (indicated on each panel if Fig. 10) and Earth's gravity, and then computed the resulting deposition velocity predicted by (33). On these plots, we have plotted the Stokes settling velocity as a function of particle radius (the dotted lines), the deposition velocity in Eq. (29) using the resistance from Zhang (2001) with $\alpha = 50$ and $\beta = 1.7$ (blue dashed lines), as well as a modified resistance where we have arbitrarily adjusted β to be 1.3 (red dashed curves). It is clear that the deposition model in Eq. (29), while practically useful, is quite sensitive to the empirical parameters α and β, and consequently, does not match the DNS data for all particle sizes, and we argue that this is due to the interpretation that the turbulent flux ignores any drift and is purely diffusive.

Furthermore, we can see that under the Zhang (2001) resistance model, the maximally enhanced particles at $St^+ = 10$ (and effective radius of $r_p \approx 2 - 3$ μm for our DNS) is also under-estimated, but for different reason than discussed above. According to the primary assumption that the resistances are added together, it is clear that their minimum value is the aerodynamic resistance R_a. However, for large Γ and $St^+ = 10$, the computed resistance is actually smaller than R_a, meaning that the enhanced settling velocity will always be under-estimated for moderate St^+ regardless of the choice of α and β. This means that the resistance-based parameterization in its current form is inadequate to describe deposition of particles with moderate St^+ and large Γ. A potential approach, but beyond the scope of the current work, would be to ascribe some Stokes number dependence on the aerodynamic drag, which in principle makes sense, as these particles may be more efficient at extracting momentum from the background turbulent flow.

Though it is beyond the scope of the current work, one could use the insight from the phase-space modeling to make modifications to (26) that may help to reconcile the results of the DNS and phenomenological model. As predicted by (21), the drift coefficient has the effect of enhancing the settling velocity for moderately sized particles. Thus the drift correction should have the effect of modifying the slope of the deposition curve where the settling is enhanced. As we see in Fig. 10a, increasing the slope of the deposition curve (red

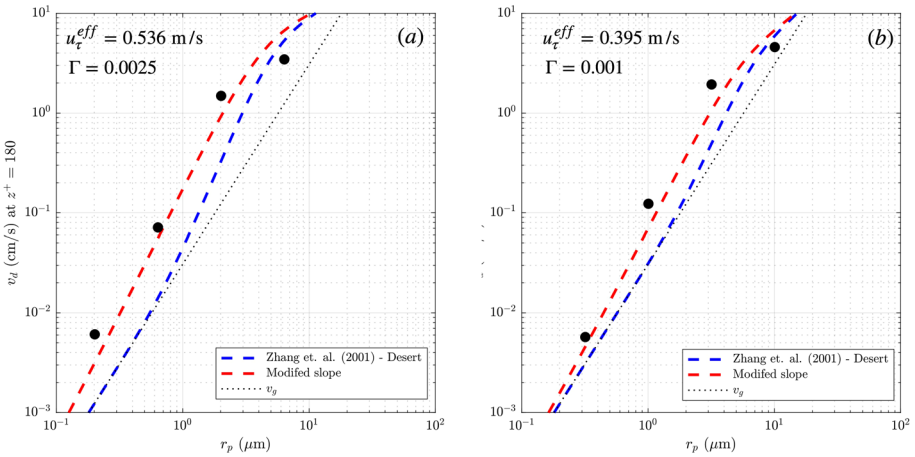

Fig. 10 Data from Table 2 re-dimensionalized and plotted as black markers to match with standard deposition curves from Hoppel (2005). The Stokes settling velocity as a function of particle radius is plotted by the dotted line. The parameterization presented in Zhang (2001) using $\beta = 1.7$ and $\alpha = 50$ (corresponding to a desert or tundra setting) is plotted by the blue dashed line. A similar parameterization with $\beta = 1.3$ and $\alpha = 50$ is shown by the red dashed curve. Panel **a** shows the case with $\Gamma = 0.001$ and panel **b** shows the case with $\Gamma = 0.0025$m and we have inlcuded the effective friction velocity implied by each value of Γ assuming Earth's gravity

dashed lines) qualitatively improves the agreement with the DNS, and as we see in Fig. 10b, at increased Γ (meaning weaker turbulence), we should expect the enhancement to be weaker. A similar approach was taken by Giardina et al. (2019), but the correction to the Stokes settling velocity was ad hoc, and approached the limit of $v_g + u_\tau$ at large St^+, which according to Fig. 3b is not true. Thus, in order to improve the predictions by the phenomenological model, a more accurate correction to the Stokes settling velocity is necessary. Furthermore, in the case of negligible gradients of mean properties ($\frac{\partial C}{\partial z}$), such as for homogeneous isotropic turbulence, we should expect the Stokes settling velocity correction to be able to reproduce the enhanced settling velocity seen in studies such as Wang and Maxey (1993), Rosa et al. (2016).

5 Discussion and Conclusions

In this work, we have coupled settling inertial Lagrangian point particles to direct numerical simulations of a turbulent boundary layer. Our goals were to identify how the independent variations in Sv^+ and St^+ modified the preferential sweeping mechanism and to use that insight to discuss two fundamentally different approaches to modeling the settling characteristics of the inertial particles. The first approach was based on the phase-space probability density of the ensemble of particles which allows us derive an exact formulation for the evolution of the average number concentration and the average particle momentum, while the second approach was a combination of a mass-conservation argument and a resistance based approach analogous to deposition models in current operational use.

First, we found that variation in Sv^+ modified the fluid velocities sampled by the particles, thus modifying the role that preferential sweeping plays in determining the settling velocity of the inertial particles. We hypothesize that particles with a given low or moderate St^+

but a larger Sv^+ sample velocities closer to the cores of turbulent eddies leading to higher sampled downward velocities within the interior of the domain. However, if Sv^+ becomes too large, they would simply move vertically through the turbulent eddies. Furthermore, when the particles attain a large enough St^+ for any Sv^+, they become ballistic and uncorrelated with the flow velocities. At this point, the velocities sampled by the particles show a negligible variation due to changes in Sv^+.

We also showed that the fluid velocities sampled by the particles were approximately normally distributed in the log-layer. For the phase-space approach, this allowed us to interpret the average fluid velocity sampled by the particles using a closure from Reeks (1992) that involves a drift component proportional to the local concentration as well as a diffusion based closure proportional to the gradient of the concentration. By focusing on the dynamics within the logarithmic region of the turbulent boundary layer, we were able to use both the DNS data and an assumption that the turbulence is approximately locally homogeneous which allowed us to constrain the diffusive and drift components of the closure. We found that the drift component was nearly an order of magnitude larger than the diffusion closure for moderate St^+ (when preferential sweeping is expected to be active), while both components were comparable in magnitude for the largest and smallest values of St^+. Furthermore, the drift coefficient captured the variations in the average settling velocities due to variations in Sv^+, thus capturing the modified preferential sweeping discussed in Fig. 4, whereas the diffusion component did not. We emphasize here that the magnitude of the drift component is nearly ten times that of the diffusion component for moderate Stokes numbers, highlighting the importance of average particle drift.

Given the insight provided in Sect. 4.2, we considered the eddy-diffusivity assumption (which ignores the drift component a priori) made in the phenomenological model of Hoppel (2005). We investigated how the deposition velocity predicted by the phenomenological approach compared to the results of the DNS. In the phenomenological model, the turbulent transport is purely diffusive and is further parameterized in terms of the aerodynamic drag (Slinn and Slinn 1980) and an empirical correction to the drag as a function of St^+ (Zhang 2001). We found that this approach represented the enhanced vertical settling velocity from the DNS in only a qualitative sense, but consistently underestimated the turbulent settling velocity, or deposition velocity, relative to the DNS. We argued that representing the turbulent transport as a purely diffusive process and ignoring net drift leads to an incorrect interpretation of the effects of the turbulence. From the insight gained in Sect. 4.2, we hypothesized that the empirical coefficients used to correct the for effects of the turbulence may in fact be trying to compensate for the drift. Therefore, in order to put the phenomenological model on stronger theoretical and physical footing, some form of drift should be included in its formulation.

It is important to note that since we are concerned with a DNS study, the Reynolds number is fairly low, thus potentially misrepresenting the settling tendencies of the largest particles. This is evident for the largest effective radii particles where the phenomenological model predicts settling velocity enhancement for 10 μm particles, while the DNS does not. This may be because the phenomenological parameterization implicitly assumes a large Reynolds number and therefore a large range of scales, including motions such as VLSMs (Smits et al. 2011). These scales, which could be responsible for enhancing the settling speed of these large particles (Tom and Bragg 2019), are absent from our DNS due to the relatively small Reynolds number.

It should also be noted that models that attempt to represent particle deposition used in mesoscale and climate modeling are even simpler than the phenomenological model discussed above. For example, see Kukkonen et al. (2012) for a comprehensive review of deposition models in operational use for regional forecasting models in Europe. Some exam-

ples of the deposition models in current use are a simple application of Stokes law, slightly more complex resistance based models (Giardina and Buffa 2018; Emerson et al. 2020), and simple gas-transfer deposition models based on Slinn and Slinn (1980). So in some sense, the phenomenological model we have considered in this paper adheres to physics in a way that operational models do not, as none of the previous models attempt to conserve aerosol mass in any way and rely on empirical corrections to match existing data.

However, these models are in common use because of their simplicity. While phase-space approach discussed in Sect. 4.2 is exact and extremely explicit in the way that it describes the role of each individual mechanism, it is complex in a way that is likely off-putting for many applied scientists. Thus, an attainable goal for the results in this work would be to use the complex phase-space models to inform and approximate simpler resistance-based models for eventual operational use. With an adequate model for γ in a turbulent boundary layer, which itself is beyond the scope of the current work, a drift correction to the Stokes settling velocity could be easily implemented in a modified phenomenological model. This represents a relatively simple but more accurate approximation that could be implemented in operational models.

Acknowledgements The authors would like to acknowledge Grant No. W911NF2220222 from the U.S. Army Research Office. The authors would also like to thank the Center for Research Computing at the University of Notre Dame, as well Tim Berk, and the two anonymous reviewers whose suggestions led to substantial improvements to the paper.

Declarations

Conflict of interest The authors report no conflict of interest

References

Aliseda A, Cartellier A, Hainaux F, Lasheras JC (2002) Effect of preferential concentration on the settling velocity of heavy particles in homogeneous isotropic turbulence. J Fluid Mech 468:77–105. https://doi.org/10.1017/S0022112002001593

Berk T, Coletti F (2020) Transport of inertial particles in high-Reynolds-number turbulent boundary layers. J Fluid Mech 903:A18. https://doi.org/10.1017/jfm.2020.597

Berk T, Coletti F (2021) Dynamics of small heavy particles in homogeneous turbulence: a Lagrangian experimental study. J Fluid Mech 917:A47. https://doi.org/10.1017/jfm.2021.280

Boudreau BP, Hill PS (2020) Rouse revisited: the bottom boundary condition for suspended sediment profiles. Mar Geol 419(106):066. https://doi.org/10.1016/j.margeo.2019.106066

Bragg A, Swailes DC, Skartlien R (2012) Drift-free kinetic equations for turbulent dispersion. Phys Rev E 86(5):056306. https://doi.org/10.1103/PhysRevE.86.056306

Bragg A, Swailes DC, Skartlien R (2012) Particle transport in a turbulent boundary layer: non-local closures for particle dispersion tensors accounting for particle-wall interactions. Phys Fluids 24(10):103304. https://doi.org/10.1063/1.4757657

Bragg AD, Richter DH, Wang G (2021) Mechanisms governing the settling velocities and spatial distributions of inertial particles in wall-bounded turbulence. Phys Rev Fluids 6(6):064302. https://doi.org/10.1103/PhysRevFluids.6.064302

Bragg AD, Richter DH, Wang G (2021) Settling strongly modifies particle concentrations in wall-bounded turbulent flows even when the settling parameter is asymptotically small. Phys Rev Fluids 6(12):124301. https://doi.org/10.1103/PhysRevFluids.6.124301

Brandt L, Coletti F (2022) Particle-laden turbulence: progress and perspectives. Annu Rev Fluid Mech 54(1):159–189. https://doi.org/10.1146/annurev-fluid-030121-021103

Csanady GT (1963) Turbulent diffusion of heavy particles in the atmosphere. J Atmos Sci 20(3):201–208. https://doi.org/10.1175/1520-0469(1963)020<0201:TDOHPI>2.0.CO;2

Emerson EW, Hodshire AL, DeBolt HM, Bilsback KR, Pierce JR, McMeeking GR, Farmer DK (2020) Revisiting particle dry deposition and its role in radiative effect estimates. Proc Natl Acad Sci 117(42):26076–26082. https://doi.org/10.1073/pnas.2014761117

Farmer DK, Boedicker EK, DeBolt HM (2021) Dry deposition of atmospheric aerosols: approaches, observations, and mechanisms. Annu Rev Phys Chem 72(1):375–397. https://doi.org/10.1146/annurev-physchem-090519-034936

Fischer HB (1973) Longitudinal dispersion and turbulent mixing in open-channel flow. Annu Rev Fluid Mech 5(1):59–78. https://doi.org/10.1146/annurev.fl.05.010173.000423

Freire LS, Chamecki M, Gillies JA (2016) Flux-profile relationship for dust concentration in the stratified atmospheric surface layer. Bound-Layer Meteorol 160(2):249–267. https://doi.org/10.1007/s10546-016-0140-2

Gao W, Samtaney R, Richter DH (2023) Direct numerical simulation of particle-laden flow in an open channel at. J Fluid Mech 957:A3. https://doi.org/10.1017/jfm.2023.26

Giardina M, Buffa P (2018) A new approach for modeling dry deposition velocity of particles. Atmos Environ 180:11–22. https://doi.org/10.1016/j.atmosenv.2018.02.038

Giardina M, Donateo A, Buffa P, Contini D, Cervone A, Lombardo C, Rocchi F (2019) Atmospheric dry deposition processes of particles on urban and suburban surfaces: modelling and validation works. Atmos Environ 214(116):857. https://doi.org/10.1016/j.atmosenv.2019.116857

Giorgi F (1986) A particle dry-deposition parameterization scheme for use in tracer transport models. J Geophys Res 91(D9):9794. https://doi.org/10.1029/JD091iD09p09794

Good G, Ireland P, Bewley G, Bodenschatz E, Collins L, Warhaft Z (2014) Settling regimes of inertial particles in isotropic turbulence. J Fluid Mech 759:R3. https://doi.org/10.1017/jfm.2014.602

Holtslag AAM, Moeng CH (1991) Eddy diffusivity and countergradient transport in the convective atmospheric boundary layer. J Atmos Sci 48(14):1690–1698. https://doi.org/10.1175/1520-0469(1991)048<1690:EDACTI>2.0.CO;2

Hoppel WA (2002) Surface source function for sea-salt aerosol and aerosol dry deposition to the ocean surface. J Geophys Res 107(D19):4382. https://doi.org/10.1029/2001JD002014

Hoppel WA (2005) Particle deposition on water: surface source versus upwind source. J Geophys Res 110(D10):D10206. https://doi.org/10.1029/2004JD005148

Ireland PJ, Bragg AD, Collins LR (2016) The effect of Reynolds number on inertial particle dynamics in isotropic turbulence. Part 2. Simulations with gravitational effects. J Fluid Mech 796:659–711. https://doi.org/10.1017/jfm.2016.227

Jenkins GS, McCauley K, Thompson T, Diokhane A (2022) WRF-CHEM simulations of unhealthy PM10 concentrations during Four Dust Events in Senegal. J Geophys Res Atmos 127:e2022JD037068

Kantha LH, Clayson CA (2000) Small scale processes in geophysical fluid flows. Elsevier, Amsterdam

Kind R (1992) One-dimensional aeolian suspension above beds of loose particles-A new concentration-profile equation. Atmos Environ A Gen Top 26(5):927–931. https://doi.org/10.1016/0960-1686(92)90250-O

Kok JF, Parteli EJR, Michaels TI, Karam DB (2012) The physics of wind-blown sand and dust. Reports Prog Phys 75(10):106901. https://doi.org/10.1088/0034-4885/75/10/106901

Kok JF, Ridley DA, Zhou Q, Miller RL, Zhao C, Heald CL, Ward DS, Albani S, Haustein K (2017) Smaller desert dust cooling effect estimated from analysis of dust size and abundance. Nat Geosci 10(4):274–278. https://doi.org/10.1038/ngeo2912

Kukkonen J, Olsson T, Schultz DM, Baklanov A, Klein T, Miranda AI, Monteiro A, Hirtl M, Tarvainen V, Boy M, Peuch VH, Poupkou A, Kioutsioukis I, Finardi S, Sofiev M, Sokhi R, Lehtinen KEJ, Karatzas K, San José R, Astitha M, Kallos G, Schaap M, Reimer E, Jakobs H, Eben K (2012) A review of operational, regional-scale, chemical weather forecasting models in Europe. Atmos Chem Phys 12(1):1–87. https://doi.org/10.5194/acp-12-1-2012

Kunkel GJ, Marusic I (2006) Study of the near-wall-turbulent region of the high-Reynolds-number boundary layer using an atmospheric flow. J Fluid Mech 548(1):375. https://doi.org/10.1017/S0022112005007780

Li C, Lim K, Berk T, Abraham A, Heisel M, Guala M, Coletti F, Hong J (2021) Settling and clustering of snow particles in atmospheric turbulence. J Fluid Mech 912:A49. https://doi.org/10.1017/jfm.2020.1153

Marchioli C, Soldati A, Kuerten J, Arcen B, Tanière A, Goldensoph G, Squires K, Cargnelutti M, Portela L (2008) Statistics of particle dispersion in direct numerical simulations of wall-bounded turbulence: Results of an international collaborative benchmark test. Int J Multiph Flow 34(9):879–893. https://doi.org/10.1016/j.ijmultiphaseflow.2008.01.009

Marusic I, Uddin AKM, Perry AE (1997) Similarity law for the streamwise turbulence intensity in zero-pressure-gradient turbulent boundary layers. Phys Fluids 9(12):3718–3726. https://doi.org/10.1063/1.869509

Maxey MR (1987) The gravitational settling of aerosol particles in homogeneous turbulence and random flow fields. J Fluid Mech 174:441–465. https://doi.org/10.1017/S0022112087000193

Miller RL, Cakmur RV, Perlwitz J, Geogdzhayev IV, Ginoux P, Koch D, Kohfeld KE, Prigent C, Ruedy R, Schmidt GA, Tegen I (2006) Mineral dust aerosols in the NASA Goddard Institute for Space Sciences ModelE atmospheric general circulation model. J Geophys Res 111(D6):D06208. https://doi.org/10.1029/2005JD005796

Nemes A, Dasari T, Hong J, Guala M, Coletti F (2017) Snowflakes in the atmospheric surface layer: observation of particle-turbulence dynamics. J Fluid Mech 814:592–613. https://doi.org/10.1017/jfm.2017.13

Nissanka ID, Park HJ, Freire LS, Chamecki M, Reid JS, Richter DH (2018) Parameterized vertical concentration profiles for aerosols in the marine atmospheric boundary layer. J Geophys Res Atmos 123(17):9688–9702. https://doi.org/10.1029/2018JD028820

Oesterlé B, Zaichik LI (2004) On Lagrangian time scales and particle dispersion modeling in equilibrium turbulent shear flows. Phys Fluids 16(9):3374–3384. https://doi.org/10.1063/1.1773844

Pope SB (2000) Turbulent flows. Cambridge University Press, Cambridge

Prandtl L (1952) Essentials of fluid dynamics: with applications to hydraulics aeronautics, meteorology, and other subjects. Hafner Publishing Company, New York

Pullin DI, Saffman PG (1998) VORTEX DYNAMICS IN TURBULENCE. Annu Rev Fluid Mech 30(1):31–51. https://doi.org/10.1146/annurev.fluid.30.1.31

Querol X, Tobías A, Pérez N, Karanasiou A, Amato F, Stafoggia M, Pérez García-Pando C, Ginoux P, Forastiere F, Gumy S, Mudu P, Alastuey A (2019) Monitoring the impact of desert dust outbreaks for air quality for health studies. Environ Int 130(104):867. https://doi.org/10.1016/j.envint.2019.05.061

Reeks MW (1991) On a kinetic equation for the transport of particles in turbulent flows. Phys Fluids A 3(3):446–456. https://doi.org/10.1063/1.858101

Reeks MW (1992) On the continuum equations for dispersed particles in nonuniform flows. Phys Fluids A 4(6):1290–1303. https://doi.org/10.1063/1.858247

Reeks MW (2021) The Development and Application of a Kinetic Theory for Modeling Dispersed Particle Flows. J Fluids Eng 143(8):080803. https://doi.org/10.1115/1.4051289

Richter D, Chamecki M (2018) Inertial effects on the vertical transport of suspended particles in a turbulent boundary layer. Bound-Layer Meteorol 167(2):235–256. https://doi.org/10.1007/s10546-017-0325-3

Rosa B, Parishani H, Ayala O, Wang LP (2016) Settling velocity of small inertial particles in homogeneous isotropic turbulence from high-resolution DNS. Int J Multiph Flow 83:217–231. https://doi.org/10.1016/j.ijmultiphaseflow.2016.04.005

Rouse H (1937) Modern conceptions of the mechanics of fluid turbulence. Trans Am Soc Civ Eng 102(1):463–505

Ryder CL, Marenco F, Brooke JK, Estelles V, Cotton R, Formenti P, McQuaid JB, Price HC, Liu D, Ausset P, Rosenberg PD, Taylor JW, Choularton T, Bower K, Coe H, Gallagher M, Crosier J, Lloyd G, Highwood EJ, Murray BJ (2018) Coarse-mode mineral dust size distributions, composition and optical properties from AER-D aircraft measurements over the tropical eastern Atlantic. Atmos Chem Phys 18(23):17225–17257. https://doi.org/10.5194/acp-18-17225-2018

Seinfeld JH, Pandis SN (1998) Atmospheric chemistry and physics: from air pollution to climate change, 1st edn. John Wiley and Sons, New York

Shao Y (2008) Dust transport and deposition. Physics and modelling of wind erosion. Springer, Dordrecht, pp 247–301

Sikovsky DP (2019) Particle Reynolds stress model for wall turbulence with inertial particle clustering. J Phys Confer Ser 1382(1):012099. https://doi.org/10.1088/1742-6596/1382/1/012099

Skartlien R (2007) Kinetic modeling of particles in stratified flow—evaluation of dispersion tensors in inhomogeneous turbulence. Int J Multiph Flow 33(9):1006–1022. https://doi.org/10.1016/j.ijmultiphaseflow.2007.04.001

Slinn S, Slinn W (1980) Predictions for particle deposition on natural waters. Atmos Environ 1967 14(9):1013–1016. https://doi.org/10.1016/0004-6981(80)90032-3

Slinn W (1967) Predictions for particle deposition to vegetative canopies. Atmos Environ 16(7):1785–1794. https://doi.org/10.1016/0004-6981(82)90271-2

Smits AJ, McKeon BJ, Marusic I (2011) High-Reynolds number wall turbulence. Annu Rev Fluid Mech 43(1):353–375. https://doi.org/10.1146/annurev-fluid-122109-160753

Tom J, Bragg AD (2019) Multiscale preferential sweeping of particles settling in turbulence. J Fluid Mech 871:244–270. https://doi.org/10.1017/jfm.2019.337

Vickers D, Mahrt L, Andreas EL (2015) Formulation of the sea surface friction velocity in terms of the mean wind and bulk stability. J Appl Meteorol Climatol 54(3):691–703. https://doi.org/10.1175/JAMC-D-14-0099.1

Wang G, Fong KO, Coletti F, Capecelatro J, Richter DH (2019) Inertial particle velocity and distribution in vertical turbulent channel flow: a numerical and experimental comparison. Int J Multiph Flow 120(103):105. https://doi.org/10.1016/j.ijmultiphaseflow.2019.103105

Wang LP, Maxey MR (1993) Settling velocity and concentration distribution of heavy particles in homogeneous isotropic turbulence. J Fluid Mech 256:27–68. https://doi.org/10.1017/S0022112093002708

Wang LP, Stock DE (1993) Dispersion of heavy particles by turbulent motion. J Atmos Sci 50(13):1897–1913. https://doi.org/10.1175/1520-0469(1993)050<1897:DOHPBT>2.0.CO;2

Wyngaard JC, Brost RA (1984) Top-down and bottom-up diffusion of a scalar in the convective boundary layer. J Atmos Sci 41(1):102–112. https://doi.org/10.1175/1520-0469(1984)041<0102:TDABUD>2.0.CO;2

Zhang L (2001) A size-segregated particle dry deposition scheme for an atmospheric aerosol module. Atmos Environ 35(3):549–560. https://doi.org/10.1016/S1352-2310(00)00326-5

Zhang Y, Bragg AD, Wang G (2023) Asymptotic closure model for inertial particle transport in turbulent boundary layers. Physical Review Fluids 8(1):014301. https://doi.org/10.1103/PhysRevFluids.8.014301